

Kpc-scale properties of dust temperature in terms of dust mass and star formation activity

I-Da Chiang (江宜達)^{1*}, Hiroyuki Hirashita^{1,2}, Jérémy Chasten³, Eric W. Koch⁴, Adam K. Leroy^{5,6}, Erik Rosolowsky⁷, Karin M. Sandstrom⁸, Amy Sardone^{5,6}, Jiayi Sun (孙嘉懿)^{9,10}, Thomas G. Williams^{11,12}

¹*Institute of Astronomy and Astrophysics, Academia Sinica, No. 1, Sec. 4, Roosevelt Road, Taipei 10617, Taiwan*

²*Theoretical Astrophysics, Department of Earth and Space Science, Osaka University, 1-1 Machikaneyama, Toyonaka, Osaka 560-0043, Japan*

³*Sterrenkundig Observatorium, Universiteit Gent, Krijgslaan 281 S9, B-9000 Gent, Belgium*

⁴*Center for Astrophysics | Harvard & Smithsonian, 60 Garden Street, Cambridge, MA 02138, USA*

⁵*Department of Astronomy, The Ohio State University, 140 West 18th Avenue, Columbus, OH 43210, USA*

⁶*Center for Cosmology and Astroparticle Physics, 191 West Woodruff Avenue, Columbus, OH 43210, USA*

⁷*Department of Physics, University of Alberta, 4-183 CCIS, Edmonton, AB T6G 2E1, Canada*

⁸*Center for Astrophysics and Space Sciences, Department of Physics, University of California, San Diego, 9500 Gilman Drive, La Jolla, CA 92093, USA*

⁹*Department of Physics and Astronomy, McMaster University, 1280 Main Street West, Hamilton, ON L8S 4M1, Canada*

¹⁰*Canadian Institute for Theoretical Astrophysics (CITA), University of Toronto, 60 St George Street, Toronto, ON M5S 3H8, Canada*

¹¹*Max-Planck-Institut für Astronomie, Königstuhl 17, D-69117 Heidelberg, Germany*

¹²*Sub-department of Astrophysics, Department of Physics, University of Oxford, Keble Road, Oxford OX1 3RH, UK*

Accepted XXX. Received YYY; in original form ZZZ

ABSTRACT

We investigate how the dust temperature is affected by local environmental quantities, especially dust surface density (Σ_{dust}), dust-to-gas ratio (D/G) and interstellar radiation field. We compile multi-wavelength observations in 46 nearby galaxies, uniformly processed with a common physical resolution of 2 kpc. A physical dust model is used to fit the infrared dust emission spectral energy distribution (SED) observed with *WISE* and *Herschel*. The star formation rate (SFR) is traced with *GALEX* ultraviolet data corrected by *WISE* infrared. We find that the dust temperature correlates well with the SFR surface density (Σ_{SFR}), which traces the radiation from young stars. The dust temperature decreases with increasing D/G at fixed Σ_{SFR} as expected from stronger dust shielding at high D/G, when Σ_{SFR} is higher than $\sim 2 \times 10^{-3} \text{ M}_{\odot} \text{ yr}^{-1} \text{ kpc}^{-2}$. These measurements are in good agreement with the dust temperature predicted by our proposed analytical model. Below this range of Σ_{SFR} , the observed dust temperature is higher than the model prediction and is only weakly dependent on D/G, which is possibly due to the dust heating from old stellar population or the variation of SFR within the past 10^{10} yr . Overall, the dust temperature as a function of Σ_{SFR} and Σ_{dust} predicted by our analytical model is consistent with observations. We also notice that at fixed gas surface density, Σ_{SFR} tends to increase with D/G, i.e. we can empirically modify the Kennicutt-Schmidt law with a dependence on D/G to better match observations.

Key words: dust, extinction – galaxies: star formation – galaxies: ISM – infrared: ISM – radiative transfer – ultraviolet: stars

1 INTRODUCTION

Dust is a key component in the interstellar medium (ISM). In the diffuse ISM of the Milky Way (MW), roughly 20–50 per cent of metals reside in solid dust grains according to elemental depletions ($F_{*} = 0$ to 1 in Jenkins 2009). Dust grains absorb and scatter a significant fraction of starlight in galaxies (e.g. 30 per cent suggested in Bernstein et al. 2002), and re-radiates the absorbed energy in the infrared (IR, Calzetti 2001; Buat et al. 2012). These processes regulate the spectral energy distribution (SED) of the interstellar radiation field (ISRF). Dust catalyzes the formation of H_2 (Gould & Salpeter 1963; Draine 2003; Cazaux & Tielens 2004; Yamasawa et al. 2011; Galliano et al. 2018), which helps the formation of the molecular phase ISM. Because of the major roles of dust in

galaxy evolution and chemistry, it is important to track the interaction between dust and the ISRF in various environments in the ISM. In particular, the dust surface density is of critical importance because it is not only an indicator of the dust mass but also is proportional to the dust optical depth.

The dust surface density (Σ_{dust}) in the ISM can be obtained by analyzing the dust emission SED in the IR (Desert et al. 1990; Draine & Li 2007; Compiègne et al. 2011; Jones et al. 2017; Relaño et al. 2020; Hensley & Draine 2022). The intensity of dust emission is proportional to the dust mass at fixed wavelength and is a monotonically increasing function of the dust temperature. The dust temperature (T_{dust}), or the radiation field heating up dust in some models, can be constrained with the ratio between dust emission at different photometric bands in the measured SED. With the obtained value for T_{dust} , we are able to derive Σ_{dust} from the intensity of dust emission with an assumption of grain emissivity.

* E-mail: idchiang@asiaa.sinica.edu.tw

With multi-band far-IR (FIR) data, especially the 70–500 μm photometry obtained with the *Herschel Space Observatory* (Pilbratt et al. 2010), there have been many efforts to measure spatially resolved, emission-based Σ_{dust} and T_{dust} in nearby galaxies (e.g. Aniano et al. 2012; Bendo et al. 2012; Smith et al. 2012; Draine et al. 2014; Gordon et al. 2014; Tabatabaei et al. 2014; Bendo et al. 2015; Davies et al. 2017; Bianchi et al. 2018; Utomo et al. 2019; Vélchez et al. 2019; Aniano et al. 2020; Chiang et al. 2021; Nersesian et al. 2021). Meanwhile, observations of distant (high-redshift) galaxies are often performed with the Atacama Large Millimeter/submillimeter Array (ALMA) because of increased requirements for spatial resolution and sensitivity (e.g. Capak et al. 2015; Watson et al. 2015; Bouwens et al. 2016; Liu et al. 2019). Due to the narrow instantaneous frequency coverage of ALMA, each galaxy is observed in a limited number of wavelength bands, usually only 1–2 bands, and as a result the dust temperatures in these systems remain comparatively uncertain. In spite of these limitations, the observed dust temperatures by ALMA have provided meaningful insight into the physical conditions in the ISM at high redshift. Studies that succeeded in obtaining multi-band ALMA data suggested that high-redshift T_{dust} spans ~ 30 – 70 K (see the $z \sim 5$ – 8.3 data compiled in Burgarella et al. 2020; Bakx et al. 2021), which is not only warmer but also showing a larger variety than the dust temperatures observed in nearby disc galaxies, e.g. ~ 17 – 40 K in the KINGFISH samples (Dale et al. 2012) and ~ 15 – 25 K in the Local Group (Utomo et al. 2019). High dust temperatures in distant galaxies are also indicated by some indirect estimates using the ultraviolet (UV) optical depth or the [C II] 158 μm line (Sommovigo et al. 2022; Ferrara et al. 2022). These results indicate that the ISRFs are high probably because of intense star formation activity in high-redshift galaxies.

In Hirashita & Chiang (2022, hereafter Paper I), we built analytical models that evaluate how dust temperature varies with relevant physical quantities, i.e. dust surface density and ISRF, to clarify the physical conditions that possibly cause the observed high and scattered T_{dust} in high-redshift galaxies. With these models, we predicted that to the first order, T_{dust} increases with UV radiation from stars (traced by the star formation rate surface density, Σ_{SFR}). This supports the above-mentioned view of intense star formation activity in high-redshift galaxies. We also found that, at fixed Σ_{SFR} , dust temperature increases towards lower dust-to-gas ratio (D/G). This is because of less shielding of ISRF by dust (see also Sommovigo et al. 2022). Moreover, with Σ_{SFR} and Σ_{dust} measured, we can roughly predict the dust temperature, which offers a way to improve the dust mass and temperature estimation iteratively. We tested these predictions against several high-redshift observations.

Although we obtained useful insights using our model, the large uncertainties and low spatial resolutions of high-redshift observations hampered rigid conclusions. Observations with greater precision and larger sample size are useful to validate our dust temperature model in Paper I. For this purpose, observations in the nearby galaxies are suitable in terms of both precision and sample size, as demonstrated by the multi-wavelength datasets in the literature (e.g. Barrera-Ballesteros et al. 2016, 2021; Casasola et al. 2017, 2022; Leroy et al. 2019; Enia et al. 2020; Morselli et al. 2020; Ellison et al. 2021; Sánchez et al. 2021; Abdurro’uf et al. 2022a; Sun et al. 2022). These observations also provide measurements at the low Σ_{SFR} and Σ_{dust} end, which was not tested in Paper I. With the availability of multi-band FIR photometric data, e.g. observations made with *Herschel*, and gas surface densities from high sensitivity emission line observations, e.g. The H I Nearby Galaxy Survey (THINGS) (Walter et al. 2008), The HERA CO-Line Extragalactic Survey (HERACLES) (Leroy et al. 2009) and the ALMA, VLA and

MeerKAT surveys conducted in the Physics at High Angular resolution in Nearby Galaxies (PHANGS) project¹ (Leroy et al. 2021b; Sun et al. 2022), we are able to derive dust temperature and D/G more robustly for nearby galaxies.

In this work, we compare our model to a sample of nearby galaxies to investigate what regulates the dust temperature. We compile spatially resolved, multi-wavelength data for 46 nearby galaxies. We uniformly process them with a 2 kpc resolution. We derive key quantities that affect the dust temperature with the following methods: Σ_{dust} is derived from the dust emission SED observed with the *Wide-field Infrared Survey Explorer* (WISE, Wright et al. 2010) and *Herschel* using the Draine & Li (2007) physical dust model including the correction factor introduced by Chasten et al. (2021). We utilize the *Galaxy Evolution Explorer* (GALEX, Martin et al. 2005) UV data, supplemented by WISE IR, to trace star formation rate (SFR) following the Leroy et al. (2019) prescription. Besides dust temperature, we also examine the scaling relations among the surface densities of dust, SFR and gas, which are necessary to setup the Paper I model. These measurements and comparisons allow us to test the model in Paper I and to clarify how key physical properties, especially star formation activity and dust surface density, regulate the dust temperature.

This paper is organized as follows. In Section 2, we introduce the sample galaxies and data sets used in this work. In Section 3, we describe how we uniformly process the multi-wavelength observations and convert them to desired physical quantities. We also outline how we adapt the Paper I model in this work. We present our measured dust temperature and relevant scaling relations in Section 4. We compare our measurements to the Paper I model and provide some extended discussions in Section 5. Finally, we summarize our key findings in Section 6.

2 SAMPLE AND DATA

The data necessary for this study are dust surface densities and temperatures from IR photometry, gas surface densities from CO and H I emission lines and SFRs from UV and IR photometry. We select our sample galaxies from the $z = 0$ Multiwavelength Galaxy Synthesis (z0MGS) catalog (Leroy et al. 2019, J. Chasten et al. in preparation). We pick the galaxies with *Herschel* IR, WISE IR and GALEX UV data available as the master sample. From this large sample, we pick 49 galaxies with both low- J CO rotational lines and H I data from archival or our new data. We set the desired physical resolution at 2 kpc, which puts a limitation on distance at $D \lesssim 20$ Mpc, corresponding to ~ 2 kpc resolution of the coarsest resolution data obtained by the *Herschel* SPIRE 250 μm band. Finally, we exclude high-inclination ($> 80^\circ$) galaxies, which yields 46 galaxies in the end.² We list the properties and data sources of these galaxies in Table 1.

2.1 Data Sets

In this section, we describe the data sets adopted in this work. All these data sets are processed with the method later described in Section 3.1.

Herschel FIR. We use *Herschel* FIR data for the dust SED fitting and calculating the colour temperature of dust emission. We adopt

¹ <http://phangs.org/>

² An early version of this data set was first compiled in Chiang (2021).

Table 1. Sample galaxies.

Galaxy	Dist. [Mpc]	i [°]	P.A. [°]	R_{25} [kpc]	R_{eff} [kpc]	$\log(M_{\star})$ [M_{\odot}]	Type	CO Ref	H I Ref	12+log(O/H) Ref
(1)	(2)	(3)	(4)	(5)	(6)	(7)	(8)	(9)	(10)	(11)
IC0342	3.4	31.0	42.0	9.9	4.3	10.2	5	<i>a.</i>	<i>h.</i>	<i>p.</i>
NGC0224	0.8	77.7	38.0	21.2	--	--	3	<i>b.</i>	<i>i.</i>	<i>r.</i>
NGC0253	3.7	75.0	52.5	14.4	4.7	10.5	5	<i>c.</i>	<i>j.</i>	--
NGC0300	2.1	39.8	114.3	5.9	2.0	9.3	6	<i>c.</i>	<i>j.</i>	<i>r.</i>
NGC0337	19.5	51.0	90.0	8.3	2.4	9.7	6	<i>d.</i>	<i>k.</i>	--
NGC0598	0.9	55.0	201.0	8.5	2.5	9.4	5	<i>e.</i>	<i>l.</i>	<i>r.</i>
NGC0628	9.8	8.9	20.7	14.1	3.9	10.2	5	<i>c.</i>	<i>m.</i>	<i>q.</i>
NGC0925	9.2	66.0	287.0	14.3	4.5	9.8	6	<i>d.</i>	<i>m.</i>	<i>r.</i>
NGC2403	3.2	63.0	124.0	9.3	2.4	9.6	5	<i>d.</i>	<i>m.</i>	<i>r.</i>
NGC2841	14.1	74.0	153.0	14.2	5.4	10.9	3	<i>d.</i>	<i>m.</i>	--
NGC2976	3.6	65.0	335.0	3.0	1.3	9.1	5	<i>d.</i>	<i>m.</i>	--
NGC3184	12.6	16.0	179.0	13.5	5.3	10.3	5	<i>d.</i>	<i>m.</i>	<i>r.</i>
NGC3198	13.8	72.0	215.0	13.0	5.0	10.0	5	<i>d.</i>	<i>m.</i>	--
NGC3351	10.0	45.1	193.2	10.5	3.0	10.3	3	<i>c.</i>	<i>m.</i>	<i>q.</i>
NGC3521	13.2	68.8	343.0	16.0	3.9	11.0	3	<i>c.</i>	<i>m.</i>	--
NGC3596	11.3	25.1	78.4	6.0	1.6	9.5	5	<i>c.</i>	<i>n.</i>	--
NGC3621	7.1	65.8	343.8	9.8	2.7	10.0	6	<i>c.</i>	<i>m.</i>	<i>r.</i>
NGC3627	11.3	57.3	173.1	16.9	3.6	10.7	3	<i>c.</i>	<i>m.</i>	<i>q.</i>
NGC3631	18.0	32.4	-65.6	9.7	2.9	10.2	5	<i>f.</i>	<i>h.</i>	--
NGC3938	17.1	14.0	195.0	13.4	3.7	10.3	5	<i>d.</i>	<i>k.</i>	--
NGC3953	17.1	61.5	12.5	15.2	5.3	10.6	4	<i>f.</i>	<i>h.</i>	--
NGC4030	19.0	27.4	28.7	10.5	2.1	10.6	4	<i>f.</i>	<i>h.</i>	--
NGC4051	17.1	43.4	-54.8	14.7	3.7	10.3	3	<i>f.</i>	<i>h.</i>	--
NGC4207	15.8	64.5	121.9	3.4	1.4	9.6	7	<i>c.</i>	<i>n.</i>	--
NGC4254	13.1	34.4	68.1	9.6	2.4	10.3	5	<i>c.</i>	<i>k.</i>	<i>q.</i>
NGC4258	7.6	68.3	150.0	18.7	5.8	10.7	4	<i>g.</i>	<i>o.</i>	<i>r.</i>
NGC4321	15.2	38.5	156.2	13.5	5.5	10.7	3	<i>c.</i>	<i>k.</i>	<i>q.</i>
NGC4450	16.8	48.5	-6.3	13.3	4.3	10.7	2	<i>f.</i>	<i>h.</i>	--
NGC4496A	14.9	53.8	51.1	7.3	3.0	9.6	6	<i>c.</i>	<i>h.</i>	--
NGC4501	16.8	60.1	-37.8	21.1	5.2	11.0	3	<i>a.</i>	<i>h.</i>	--
NGC4536	16.2	66.0	305.6	16.7	4.4	10.2	3	<i>c.</i>	<i>k.</i>	--
NGC4559	8.9	65.0	328.0	13.7	3.5	9.8	5	<i>g.</i>	<i>o.</i>	--
NGC4569	15.8	70.0	18.0	20.9	5.9	10.8	2	<i>c.</i>	<i>k.</i>	--
NGC4625	11.8	47.0	330.0	2.4	1.2	9.1	9	<i>d.</i>	<i>k.</i>	<i>r.</i>
NGC4651	16.8	50.1	73.8	9.5	2.4	10.3	5	<i>f.</i>	<i>h.</i>	<i>r.</i>
NGC4689	15.0	38.7	164.1	8.3	4.7	10.1	5	<i>c.</i>	<i>h.</i>	--
NGC4725	12.4	54.0	36.0	17.5	6.0	10.8	1	<i>d.</i>	<i>k.</i>	--
NGC4736	4.4	41.0	296.0	5.0	0.8	10.3	1	<i>d.</i>	<i>m.</i>	--
NGC4826	4.4	59.1	293.6	6.7	1.5	10.2	1	<i>c.</i>	<i>m.</i>	--
NGC4941	15.0	53.4	202.2	7.3	3.4	10.1	1	<i>c.</i>	<i>h.</i>	--
NGC5055	9.0	59.0	102.0	15.5	4.2	10.7	4	<i>d.</i>	<i>m.</i>	--
NGC5248	14.9	47.4	109.2	8.8	3.2	10.3	3	<i>c.</i>	<i>n.</i>	--
NGC5457	6.6	18.0	39.0	23.2	13.4	10.3	5	<i>d.</i>	<i>m.</i>	<i>r.</i>
NGC6946	7.3	33.0	243.0	12.2	4.5	10.5	5	<i>d.</i>	<i>m.</i>	<i>r.</i>
NGC7331	14.7	76.0	168.0	19.8	3.7	11.0	4	<i>d.</i>	<i>m.</i>	--
NGC7793	3.6	50.0	290.0	5.5	1.9	9.3	6	<i>c.</i>	<i>m.</i>	<i>r.</i>

Notes: (2) Distance (from EDD Tully et al. 2009); (3–4) inclination angle and position angle (Sofue et al. 1999; de Blok et al. 2008; Leroy et al. 2009; Muñoz-Mateos et al. 2009b; Meidt et al. 2009; Corbelli et al. 2010; McCormick et al. 2013; Faesi et al. 2014; Makarov et al. 2014; Koch et al. 2018; Lang et al. 2020); (5) isophotal radius (Makarov et al. 2014); (6) effective radius (Leroy et al. 2021b); (7) logarithmic global stellar mass (Leroy et al. 2019); (8) numerical Hubble stage T; (9) References of CO observations. *a.* Kuno et al. (2007); *b.* Nietten et al. (2006); *c.* PHANGS-ALMA (Leroy et al. 2021b); *d.* HERACLES (Leroy et al. 2009); *e.* Gratier et al. (2010) and Druard et al. (2014); *f.* Leroy et al. (2022); *g.* COMING (Sorai et al. 2019); (10) References of H I observations. *h.* EveryTHINGS (P.I. Sandstrom; Chiang et al. in preparation); *i.* Braun et al. (2009); *j.* Puche et al. (1991); *k.* Schrubba et al. (2011); *l.* Koch et al. (2018); *m.* THINGS (Walter et al. 2008); *n.* PHANGS-VLA (P.I. Utomo; Sardone et al. in preparation); *o.* HALOGAS (Heald et al. 2011); (11) References of 12+log(O/H) measurement. *p.* private communication with K. Kreckel (see Chiang et al. 2021); *q.* 12+log(O/H) radial gradients from PHANGS-MUSE (Santoro et al. 2022); *r.* lines from Zurita et al. (2021) compilation.

the *Herschel* FIR maps from the J. Chasten et al. (in preparation) background-subtracted data products. J. Chasten et al. (in preparation) uniformly reduced the six *Herschel* photometric bands for a large sample (~ 800) of nearby galaxies, using the Scanamorphos (Roussel 2013) routine. This includes the 70, 100, and 160 μm bands

from the Photoconductor Array Camera and Spectrometer (PACS; Poglitsch et al. 2010), and the 250, 350, and 500 μm bands from the Spectral and Photometric Imaging Receiver (SPIRE; Griffin et al. 2010). In this work, we adopt the 70 to 250 μm data products, which yields the raw point spread function (PSF) with FWHM $\sim 18''$. We

convolve the maps to a circular Gaussian PSF with FWHM of $21''$, which is the ‘moderate Gaussian’ suggested by [Aniano et al. \(2011\)](#).

GALEX UV. We use the two bands of *GALEX* at $\lambda \sim 154$ nm and $\lambda \sim 231$ nm (hereafter FUV and NUV, respectively) to trace Σ_{SFR} . We use the data products at $15''$ resolution from the zOMGS catalog ([Leroy et al. 2019](#)).

WISE near- and mid-IR. We use the data at $\lambda \sim 3.4, 4.6, 12$ and $22 \mu\text{m}$ observed by *WISE* to trace dust emission in the near- and mid-IR. We also use the 3.4 and $22 \mu\text{m}$ bands (hereafter W1 and W4, respectively) to trace Σ_{\star} and Σ_{SFR} (the latter is supplemented by the *GALEX* UV data). We use the background-subtracted data products at $15''$ resolution from the zOMGS collaboration ([Leroy et al. 2019](#)).

CO rotational lines. We use the CO rotational lines as a tracer for molecular gas. For the majority of our sample galaxies, we use the compilation of CO mapping assembled by [Leroy et al. \(2021a, 2022\)](#) from publicly available CO $J = 1 \rightarrow 0$ and $J = 2 \rightarrow 1$ data:

- CO $J = 1 \rightarrow 0$ data from the CO Multi-line Imaging of Nearby Galaxies (COMING) survey ([Sorai et al. 2019; Kuno et al. 2007](#)).
- CO $J = 2 \rightarrow 1$ data from HERACLES ([Leroy et al. 2009](#)), the PHANGS-ALMA survey ([Leroy et al. 2021b](#)), the IRAM M33 CO(2–1) survey ([Gratier et al. 2010; Druard et al. 2014](#)), and a new set of data observed by the IRAM 30 m telescope focused on the Virgo Cluster (P.I. Schrubba; processed in [Leroy et al. 2022](#)).

For NGC 224 (M31), we adopt the CO $J = 1 \rightarrow 0$ data observed with the IRAM 30-m telescope by [Nieten et al. \(2006\)](#). We obtain the map from the supplementary material³ of [Draine et al. \(2014\)](#). All the measurements adopted in this work target the $^{12}\text{C}^{16}\text{O}$ isotope only. The detailed reference for each target galaxy is listed in Table 1.

For uniformity, we convert the CO $J = 2 \rightarrow 1$ intensity to CO $J = 1 \rightarrow 0$ with the mean values of the line ratio (R_{21}) measured for this sample in [Leroy et al. \(2022\)](#):

$$I_{\text{CO } J=1 \rightarrow 0} = I_{\text{CO } J=2 \rightarrow 1} / R_{21}, \quad R_{21} = 0.65^{+0.18}_{-0.14}. \quad (1)$$

For simplicity, I_{CO} stands for $I_{\text{CO } J=1 \rightarrow 0}$ hereafter. In the main analysis, we will use the constant $R_{21} = 0.65$ as the fiducial value. Meanwhile, recent studies have attempted to formulate the variation of R_{21} as a function of local physical conditions, e.g. Σ_{SFR} . This variation has a minor effect on this work, which will be discussed in Appendix B.

H I 21 cm line. We use H I 21 cm line emission to trace the atomic gas surface density in the ISM. Detailed references for each galaxy are listed in Table 1. We include several new and publicly available H I moment 0 maps. The two new surveys, EveryTHINGS and PHANGS-VLA, used the Karl G. Jansky Very Large Array (VLA).⁴ The EveryTHINGS survey ([Chiang et al. 2021](#), in preparation) observed 39 nearby galaxies with the C and D configuration of the VLA. The typical beam size of these cubes is $\sim 20''$. For the descriptions of observation design, data reduction and imaging processes, we refer the readers to [Chiang \(2021, Chapter 4.A; I.](#)

Chiang et al. in preparation). The PHANGS-VLA (P.I. Utomo; [Sun et al. 2020](#), A. Sardone et al. in preparation) survey observed nearby galaxies in the PHANGS catalog, with similar data reduction and imaging approaches as EveryTHINGS.

Oxygen abundance. We derive the oxygen abundance as a function of galactocentric distance by adopting the radial gradient of $12+\log(\text{O}/\text{H})$ obtained from measurements in H II regions, where oxygen atoms locked in the solid phase are negligible ([Peimbert & Peimbert 2010](#)); that is, the $12+\log(\text{O}/\text{H})$ measured in H II regions represents the total $12+\log(\text{O}/\text{H})$. We use the $12+\log(\text{O}/\text{H})$ gradient or $12+\log(\text{O}/\text{H})$ measurements from the following sources: (1) The PHANGS-MUSE survey ([Emsellem et al. 2022](#)). They use strong line measurements with the Pilyugin & Grebel (2016) S-calibration⁵ (hereafter PG16S). We adopt the derived radial gradients from [Santoro et al. \(2022\)](#). (2) The optical H II region emission line compilation in [Zurita et al. \(2021\)](#). We use their catalog to calculate the PG16S $12+\log(\text{O}/\text{H})$ in H II regions and then fit the radial $12+\log(\text{O}/\text{H})$ gradient in each galaxy. We only consider galaxies that have at least 5 measurements spanning at least $0.5R_{25}$, where R_{25} is the isophotal radius at the *B*-band surface brightness $\mu_B = 25 \text{ mag arcsec}^{-2}$.

For galaxies without $12+\log(\text{O}/\text{H})$ measurements in [Zurita et al. \(2021\)](#) or [Santoro et al. \(2022\)](#), we use the two-step strategy proposed by [Sun et al. \(2020\)](#) to estimate their $12+\log(\text{O}/\text{H})$. First, we use a mass-metallicity relation⁶ to predict $12+\log(\text{O}/\text{H})$ at one effective radius (R_{eff} , the radius within which half of the galaxy’s luminosity is contained, measured with I_{W1}). Secondly, we extend the prediction with a radial gradient of $-0.1 \text{ dex}/R_{\text{eff}}$ suggested by [Sánchez et al. \(2014\)](#). We characterize the mass-metallicity relation following [Moustakas et al. \(2011, also see Sánchez et al. \(2013, 2019\)\)](#):

$$12 + \log(\text{O}/\text{H}) = a + bxe^{-x}, \quad (2)$$

where $x = \log(M_{\star}/M_{\odot}) - 11.5$, and a and b are free parameters. We obtain the best fit parameters $a = 8.56 \pm 0.02$ and $b = 0.010 \pm 0.002$ by the fit to the relation between $12+\log(\text{O}/\text{H})$ at R_{eff} and $\log(M_{\star}/M_{\odot})$ for the galaxies in Table 1.

2.2 Signal mask

In the analysis, we mask out data points with low signal-to-noise ratios in key data. The selection criteria are listed below:

- We keep pixels with $> 1\sigma$ detections in the *WISE* and *Herschel* IR bands used for dust fitting. The change in the statistics of T_{dust} is minor compared to a 3σ mask; thus we use the 1σ mask to include more data points. This also ensures the validity of the estimated colour temperature (Section 3.2). This masking is done by J. Chasten et al. (in preparation).

- We focus on regions with CO detections. We set the detection threshold to be $I_{\text{CO}} \sim 0.4 \text{ K km s}^{-1}$, which corresponds to $\Sigma_{\text{mol}} \sim 1.7 \times 10^6 M_{\odot} \text{ kpc}^{-2}$.

Most pixels passing the two criteria above are in the inner galaxy. The median radius of the pixel-by-pixel measurements is $\sim 0.4R_{25}$. There are ~ 1.6 per cent of data points with CO detection but no H I detection. For these pixels, we set their H I intensity to zero and keep

³ <https://www.astro.princeton.edu/~draine/m31dust/m31dust.html>

⁴ The VLA is operated by the National Radio Astronomy Observatory (NRAO), which is a facility of the National Science Foundation operated under cooperative agreement by Associated Universities, Inc.

⁵ They utilize the $S_2 = I_{[\text{S II}]} \lambda 6717 + \lambda 6731 / I_{H\beta}$, $N_2 = I_{[\text{N II}]} \lambda 6548 + \lambda 6584 / I_{H\beta}$, and $R_3 = I_{[\text{O III}]} \lambda 4959 + \lambda 5007 / I_{H\beta}$ line intensity ratios

⁶ Mass-metallicity relation is the scaling relation between stellar mass and gas-phase metallicity.

them in the analysis. These pixels have their Σ_{mol} span $\sim 2.7 \times 10^6 - 11.4 \times 10^6 \text{ M}_{\odot} \text{ kpc}^{-2}$, which is at least one order of magnitude above the weakest detection of Σ_{atom} in our dataset ($\sim 10^5 \text{ M}_{\odot} \text{ kpc}^{-2}$). Thus these regions should still be H_2 -dominated even if there is undetected H I existing.

3 METHOD

3.1 Multi-wavelength Data Processing

All multi-wavelength data are convolved to a Gaussian PSF with an FWHM corresponding to 2 kpc, using the `astropy.convolution` package (Astropy Collaboration et al. 2013, 2018, 2022). The images are then reprojected to a pixel size of one third of the FWHM (i.e. we oversample at roughly the Nyquist sampling rate) with the `astropy` affiliated package `reproject`. All the surface density and surface brightness quantities presented in this work have been corrected for inclination.

We blank a few regions where the emission from a foreground or background source may be confused with the main target. In NGC 4496A, we blank the region around NGC 4496B because while the IR maps detect the dust emission from NGC 4496B, the CO and H I emission from NGC 4496B are not in the spectral coverage of the available cubes. For all *GALEX* and *WISE* maps, we blank the regions with known stars in the masks compiled in the *z0MGS* database. We interpolate the intensities in the blanked regions with a circular Gaussian kernel (FWHM = $22.5''$) with the function `interpolate_replace_nans` in the `astropy.convolution` module. This interpolation is applied to the *WISE* and *GALEX* maps before convolution and reproject.

3.2 Physical Parameter Estimates

Colour temperature. In order to directly compare our measurements with the model prediction in Paper I, we use the colour temperature, which is also adopted by Paper I, as our fiducial dust temperature in the analysis. We calculate the colour temperature at two wavelengths λ_1 and λ_2 , $T_{\text{clr}}(\lambda_1, \lambda_2)$, in each pixel by solving the following equation:

$$\frac{\kappa(\lambda_1)B_{\nu}(\lambda_1, T_{\text{clr}}(\lambda_1, \lambda_2))}{\kappa(\lambda_2)B_{\nu}(\lambda_2, T_{\text{clr}}(\lambda_1, \lambda_2))} = \frac{I_{\nu}(\lambda_1)}{I_{\nu}(\lambda_2)}, \quad (3)$$

where $\kappa(\lambda)$ is the dust emissivity as a function of wavelength λ , and $I_{\nu}(\lambda)$ is the measured SED. We adopt a power-law approximation for $\kappa(\lambda)$ as

$$\kappa(\lambda) = \kappa_0 \left(\frac{\lambda_0}{\lambda} \right)^{\beta}, \quad (4)$$

where λ_0 is the reference wavelength, κ_0 is the emissivity at λ_0 and β is the power-law index. This approximation is valid in the FIR and used in MBB models (e.g. Schwartz 1982; Hildebrand 1983; Gordon et al. 2014; Chiang et al. 2018; Utomo et al. 2019). We adopt $\beta = 2$, $\lambda_0 = 160 \mu\text{m}$ and $\kappa_0 = 10.1 \text{ cm}^2 \text{ g}^{-1}$ (Chiang et al. 2018). Since the emissivity described in equation (4) is only used in calculating T_{clr} (equation 3), the values of λ_0 and κ_0 do not affect the results in this work.

Our methodology for calculating $T_{\text{clr}}(\lambda_1, \lambda_2)$ is the same as the one used in Paper I, except that we select a set of (λ_1, λ_2) more suitable for nearby galaxy observations. Specifically, we adopt $\lambda_1 = 100 \mu\text{m}$ and $\lambda_2 = 250 \mu\text{m}$ from *Herschel* PACS 100 μm and

SPIRE 250 μm data. We adopt the same set of wavelengths when we calculate T_{clr} using the Paper I model, which is to be compared with the observationally derived T_{clr} . As shown in Paper I, the colour temperature is not sensitive to the choice of wavelengths as long as we choose two wavelengths in the FIR range, which is appropriate for the *Herschel* bands. The T_{clr} scales with dust temperature derived from dust SED fitting, which we will discuss in Appendix A.

Dust surface density and ISRF. We adopt the maps of dust properties from J. Chasten et al. (in preparation). J. Chasten et al. (in preparation) fit the *WISE* (3.4, 4.6, 12 and 22 μm) and *Herschel* (70, 100, 160 and 250 μm) dust emission SED with the Draine & Li (2007) physical dust model (with the renormalized dust opacity derived in Chasten et al. 2021). The fitting is done with the Bayesian fitting tool `DustBFF` (Gordon et al. 2014). The data products include maps of dust mass surface density (Σ_{dust}), ISRF, and the fraction of polycyclic aromatic hydrocarbons (q_{PAH}). We use Σ_{dust} in our main analysis and the ISRF in Appendix A. Like the *Herschel* maps, the dust maps have raw resolution FWHM $\sim 18''$, and we convolve them to a circular Gaussian PSF with FWHM of $21''$.

SFR surface density. We use UV+IR ‘hybrid’ tracers for Σ_{SFR} with coefficients calibrated with GSWLC data (Salim et al. 2016, 2018) in the *z0MGS* project (Leroy et al. 2019). This methodology corrects the dust attenuation in the UV with IR data, thus it offers better constraint on SFR than single-band tracers. We use *GALEX* FUV or NUV and *WISE* W4 data to trace the Σ_{SFR} . For galaxies with both FUV and W4 available, we use:

$$\frac{\Sigma_{\text{SFR}}}{1 \text{ M}_{\odot} \text{ yr}^{-1} \text{ kpc}^{-2}} = 8.85 \times 10^{-2} \frac{I_{\text{FUV}}}{1 \text{ MJy sr}^{-1}} + 3.02 \times 10^{-3} \frac{I_{\text{W4}}}{1 \text{ MJy sr}^{-1}}. \quad (5)$$

For NGC 3596, for which FUV is unavailable but NUV and W4 are available, we use

$$\frac{\Sigma_{\text{SFR}}}{1 \text{ M}_{\odot} \text{ yr}^{-1} \text{ kpc}^{-2}} = 8.94 \times 10^{-2} \frac{I_{\text{NUV}}}{1 \text{ MJy sr}^{-1}} + 2.63 \times 10^{-3} \frac{I_{\text{W4}}}{1 \text{ MJy sr}^{-1}}. \quad (6)$$

For NGC 3953 and NGC 4689, for which only W4 is available, we use

$$\frac{\Sigma_{\text{SFR}}}{1 \text{ M}_{\odot} \text{ yr}^{-1} \text{ kpc}^{-2}} = 3.81 \times 10^{-3} \frac{I_{\text{W4}}}{1 \text{ MJy sr}^{-1}}. \quad (7)$$

While it is a frequently used strategy, we remind the readers that there is possible higher-order polynomial dependence on the IR term (e.g. Buat et al. 2005), and that the coefficients for the IR term depends on the dust attenuation data or model used for calibration. For further discussions about the advantages and disadvantages of SFR tracers, we refer the readers to the Kennicutt & Evans (2012, Chapter 3) review.

Stellar mass surface density. We use *WISE* W1 data to trace stellar mass surface density (Σ_{\star}) with the conversion formula suggested by *z0MGS* (Leroy et al. 2019, see their Appendix A):

$$\frac{\Sigma_{\star}}{1 \text{ M}_{\odot} \text{ kpc}^{-2}} = 3.3 \times 10^8 \left(\frac{\Upsilon_{\star}^{3.4}}{0.5 \text{ M}_{\odot} \text{ L}_{\odot}^{-1}} \right) \frac{I_{\text{W1}}}{1 \text{ MJy sr}^{-1}}, \quad (8)$$

where $\Upsilon_{\star}^{3.4}$ is stellar-to-W1 mass-to-light ratio determined from the specific SFR (sSFR)-like quantity calibration (using $\Sigma_{\text{SFR-to-}I_{\text{W1}}}$) described in [Leroy et al. \(2019\)](#).

Metallicity. We use the oxygen abundance, $12+\log(\text{O}/\text{H})$, to trace metallicity (Z). We assume a fixed abundance pattern. The conversion from $12+\log(\text{O}/\text{H})$ to metallicity relative to solar abundance is described as

$$Z' = 10^{12+\log(\text{O}/\text{H})-8.69}, \quad (9)$$

where Z' indicates the metallicity normalized to solar, and 8.69 is the solar value of $12+\log(\text{O}/\text{H})$ ([Asplund et al. 2009](#)).

Atomic Gas Surface Density. We trace the atomic gas surface density (Σ_{atom}) with the H I 21 cm line emission ($I_{\text{H I}}$) data, assuming that the opacity is negligible (e.g. [Walter et al. 2008](#)):

$$\frac{\Sigma_{\text{atom}}}{1 \text{ M}_{\odot} \text{ kpc}^{-2}} = 1.36 \times (1.46 \times 10^4) \frac{I_{\text{H I}}}{1 \text{ K km s}^{-1}}, \quad (10)$$

where the factor 1.36 accounts for the mass of helium. Note that in this work, we use the unit $\text{M}_{\odot} \text{ kpc}^{-2}$ for surface densities for more straightforward comparison with simulations instead of $\text{M}_{\odot} \text{ pc}^{-2}$, which is more commonly used in observations.

Molecular Gas Surface Density. We calculate the molecular gas surface density (Σ_{mol}) with the integrated intensity of $\text{CO } J = 1 \rightarrow 0$ line (I_{CO}) and a CO-to- H_2 conversion factor (α_{CO}):⁷

$$\frac{\Sigma_{\text{mol}}}{1 \text{ M}_{\odot} \text{ kpc}^{-2}} = \frac{\alpha_{\text{CO}}}{1 \text{ M}_{\odot} \text{ pc}^{-2} (\text{K km s}^{-1})^{-1}} \times \frac{I_{\text{CO}}}{1 \text{ K km s}^{-1}} \times 10^6, \quad (11)$$

where the 10^6 factor converts $\text{M}_{\odot} \text{ pc}^{-2}$ to $\text{M}_{\odot} \text{ kpc}^{-2}$. Throughout the paper, α_{CO} is quoted for the $\text{CO } J = 1 \rightarrow 0$ line at 115 GHz and includes a factor of 1.36 to account for helium.

We can then calculate the gas surface density (Σ_{gas}) as:

$$\Sigma_{\text{gas}} = \Sigma_{\text{atom}} + \Sigma_{\text{mol}}. \quad (12)$$

We also calculate the total surface density (Σ_{Total}), which is the combination of surface densities of stellar mass and neutral gas mass (neglecting dust mass, following [Bolatto et al. \(2013\)](#)) for calculating α_{CO} later:

$$\Sigma_{\text{Total}} = \Sigma_{\text{gas}} + \Sigma_{\star}. \quad (13)$$

How α_{CO} depends on local conditions is still an active field of study. In a simplified picture, the value of α_{CO} depends on the fraction of molecular gas without CO emission (the CO-dark gas; e.g. [Wolfire et al. 2010](#); [Glover & Mac Low 2011](#); [Leroy et al. 2011](#)) and the temperature, opacity, and density of the molecular gas. The latter terms often combine to yield enhanced CO emission in galaxy centres (e.g. [Sandstrom et al. 2013](#)) and (ultra)luminous IR galaxies. We refer the readers to the [Bolatto et al. \(2013\)](#) review for a full discussion of α_{CO} . In [Chiang et al. \(2021\)](#), we have demonstrated that to obtain spatially resolved dust-to-metals ratio (and thus D/G)

⁷ The conventional MW conversion factor is $\alpha_{\text{CO}} = 4.35 \text{ M}_{\odot} \text{ pc}^{-2} (\text{K km s}^{-1})^{-1}$ (including a factor of 1.36 for helium mass). This is equivalent to $X_{\text{CO}} = 2 \times 10^{20} \text{ cm}^{-2} (\text{K km s}^{-1})^{-1}$ in column density units (column density for H_2 only). α_{CO} can be converted to X_{CO} units by multiplying by a factor of $(\text{M}_{\odot}/2 \cdot 1.36 m_{\text{H}}) (\text{cm}^2/\text{pc}^2) = 4.6 \times 10^{19}$, where m_{H} is the mass of hydrogen atom.

with reasonable dependence on the local environment, one needs to adopt a conversion factor prescription that takes into account the enhancement of CO emission in galaxy centres. In this work, we adopt the α_{CO} formula suggested by [Bolatto et al. \(2013\)](#), which includes the enhancement of CO emission with total surface density:

$$\frac{\alpha_{\text{CO}}}{1 \text{ M}_{\odot} \text{ pc}^{-2} (\text{K km s}^{-1})^{-1}} = 2.9 \times \exp\left(\frac{0.4}{Z'}\right) \times \begin{cases} \left(\frac{\Sigma_{\text{Total}}^{100}}{1}\right)^{-0.5} & , \Sigma_{\text{Total}}^{100} \geq 1 \\ 1 & , \Sigma_{\text{Total}}^{100} < 1 \end{cases}, \quad (14)$$

where $\Sigma_{\text{Total}}^{100}$ is Σ_{Total} in units of $100 \text{ M}_{\odot} \text{ pc}^{-2}$. Note that we calculate α_{CO} iteratively because Σ_{Total} depends on α_{CO} . We start the loop with an initial value of $\alpha_{\text{CO}} = 4.35 \text{ M}_{\odot} \text{ pc}^{-2} (\text{K km s}^{-1})^{-1}$ and iterate until the current α_{CO} converges to within 1% of the previous one. We will examine the possible changes to our results with other α_{CO} prescriptions in Appendix B.

Dust-to-Gas Ratio. We calculate the D/G as

$$\text{D/G} \equiv \Sigma_{\text{dust}}/\Sigma_{\text{gas}}. \quad (15)$$

3.3 Data Weighting

In this work, we perform pixel-by-pixel analyses with our measurements. For the key quantity in this paper, dust temperature, we weight the measurements by their Σ_{dust} in the calculations of all statistical quantities, i.e. percentiles, regressions and correlation coefficients, to have the statistics reflecting the averaged properties for the dust component. For all the other analysis, we use a uniform weighting in the statistics (mainly the scaling relation between Σ_{SFR} and Σ_{dust} in Section 4.2).

3.4 Theoretical models for dust temperature (Paper I)

In Section 5, we compare our measurements to the dust temperature predicted by the model described in [Paper I](#). Here we briefly review the model and refer the reader to [Paper I](#) for details. To derive the relations between dust temperature and local physical conditions, we consider the following two models that can be treated analytically: (i) radiative transfer (RT) and (ii) one-temperature (one- T) models. In the RT model, we put stars in the midplane of the disc and the dust in a screen geometry. In this model, the temperature gradient in the direction perpendicular to the disc plane naturally emerges, so that the model is suitable for investigating a multi-temperature effect for the dust. In the one- T model, we assume that dust and stars are well mixed, so that the dust temperature is assumed to have a single value determined by the global balance between the absorbed and radiated energy by the dust. These two extremes serve to bracket the most realistic scenario. The radiation field from stars is given based on the gas mass surface density assuming the Kennicutt-Schmidt law ([Kennicutt 1998](#); [Kennicutt & Evans 2012](#); [Kennicutt & De Los Reyes 2021](#), hereafter the KS law). The KS law links Σ_{SFR} and Σ_{gas} through the following formula:

$$\log\left(\frac{\Sigma_{\text{SFR}}}{1 \text{ M}_{\odot} \text{ yr}^{-1} \text{ kpc}^{-2}}\right) = \log A + N \log\left(\frac{\Sigma_{\text{gas}}}{1 \text{ M}_{\odot} \text{ kpc}^{-2}}\right), \quad (16)$$

where A and N are free parameters.

In the RT model, we solve the radiative transfer equation in plane-parallel geometry under given values of Σ_{gas} and D/G. For simplicity, we assume a uniform disc that extends infinitely in the plane of the

galaxy (or equivalently the disc is much thinner than its horizontal extent). As mentioned in Paper I, this simplification does not have any essential impact on the results, since the corresponding geometric factor only weakly affects the resulting dust temperature. The intrinsic SED of the stellar population is calculated based on a continuous, constant Σ_{SFR} throughout a period τ_* , using STARBURST99 (Leitherer et al. 1999) with standard parameters. Starting with this intrinsic SED at the mid-plane of the disc, the RT model solves the radiative transfer equation for dust absorption in the direction perpendicular to the disc plane (i.e. in each dust layer parallel to the disc plane), and the dust temperature in each dust layer is calculated based on the radiative equilibrium. Finally, the dust emission from all layers are integrated to obtain the total dust emission SED, $I_{\text{dust}}^{\text{RT}}(\nu)$ (surface luminosity). The colour temperature of the dust emission SED is calculated by equation (3) by substituting $I_{\nu}(\lambda)$ with $I_{\text{dust}}^{\text{RT}}(\nu)$.

The results of these models are briefly summarized as follows. With a given value of D/G, the dust temperature rises with Σ_{SFR} and Σ_{dust} (which also increases with Σ_{SFR} because of the KS law). The $T_{\text{clr}}-\Sigma_{\text{SFR}}$ and $T_{\text{clr}}-\Sigma_{\text{dust}}$ relations depend on D/G in such a way that lower values of D/G lead to higher dust temperatures. The RT and one- T models predict similar colour temperatures with the same set of Σ_{dust} and Σ_{SFR} . In particular, the results of the two models are almost identical in the parameter ranges appropriate for the sample in this paper. Thus, we concentrate on the RT model only, and we provide a summary of the model setup in what follows.

In this work, there are some modifications from Paper I. Considering that the typical stellar ages of our nearby sample is older than those of the high-redshift sample in Paper I, we recalculate the intrinsic stellar SED with $\tau_* = 10$ Gyr, which is a typical age of nearby galaxies. Indeed, this choice of τ_* is equivalent to $\text{sSFR} \sim 10^{-10} \text{ yr}^{-1}$, which is consistent with our sample (Section 5.3). However, as shown in Paper I, the resulting dust temperatures are not sensitive to τ_* , so that the change of τ_* by a factor of 2 (comparable to the dispersion of sSFR) does not affect our discussions and conclusions.

Another modification from Paper I is the adopted KS law coefficients. With $\Sigma_{\text{dust}} = (\text{D/G})\Sigma_{\text{gas}}$ and the KS law, we connect the two key quantities that govern the dust temperature in the model, Σ_{SFR} and Σ_{dust} , as $\Sigma_{\text{SFR}} \propto [\Sigma_{\text{dust}}/(\text{D/G})]^N$. For the consistency with the adopted data set in this work, instead of using the fiducial coefficients in Paper I,⁸ we will use the coefficients and functional form that fit best for our data set. The details will be described in Section 4.2.

As noted above, we change one of the wavelengths selected for calculating the colour temperature (Section 3.2). In Paper I, we used $\lambda_1 = 100 \mu\text{m}$ and $\lambda_2 = 200 \mu\text{m}$ as the wavelengths are near to ALMA bands for galaxies at $z > 5$. In this work, we select wavelengths $\lambda_1 = 100 \mu\text{m}$ and $\lambda_2 = 250 \mu\text{m}$ for the comparison with the photometry data in *Herschel* PACS and SPIRE bands, respectively.

4 RESULTS

4.1 The measured dust temperature

We present the measurements for dust temperature (traced with T_{clr}) in this subsection. We first investigate the primary dependence of T_{clr} on the local physical conditions, and then look for possible secondary dependence once the primary dependence is removed.

In Table 2, we show Pearson's correlation coefficient (ρ) between T_{clr} and each of the quantities available in our analysis. Since most quantities have certain radial dependence, we include R_g/R_{25} as a

Table 2. Correlation between T_{clr} and local conditions. We calculate the Pearson's correlation coefficient (ρ) along with the p -value of the correlation.

Quantity	Pearson's ρ with T_{clr}	p -value
Σ_{atom}	0.13	$\ll 0.001$
$\log(\Sigma_{\text{mol}})$	0.67	$\ll 0.001$
$\log(\Sigma_{\text{gas}})$	0.66	$\ll 0.001$
$\log(\Sigma_{\text{SFR}})$	0.89	$\ll 0.001$
$\log(\Sigma_{\text{dust}})$	0.61	$\ll 0.001$
$\log(\text{D/G})$	0.05	0.543
$\log(\Sigma_*)$	0.67	$\ll 0.001$
$12+\log(\text{O/H})$	0.49	$\ll 0.001$
R_g/R_{25}	-0.58	$\ll 0.001$

Notes: (a) We consider the correlation as significant when we have $p < 0.05$.

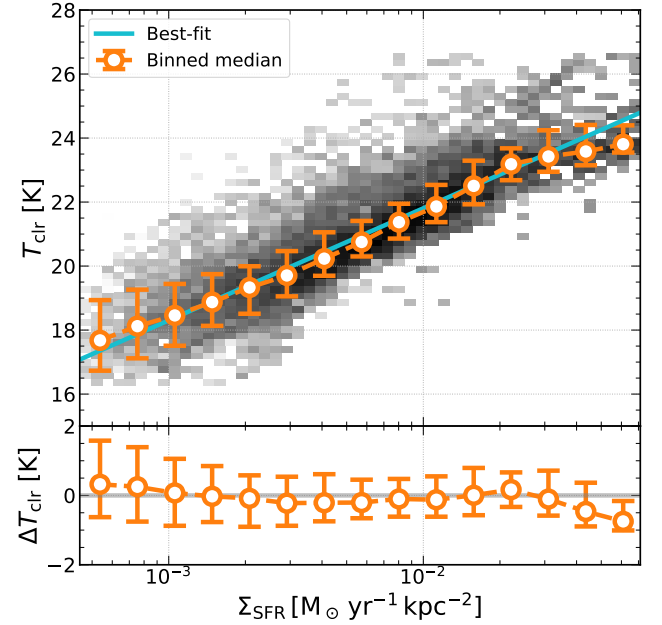


Figure 1. Measured scaling relation between T_{clr} and Σ_{SFR} . Top panel: T_{clr} displayed as a function of Σ_{SFR} . The gray scale shows the density of data points. The orange circles show the median T_{clr} in each Σ_{SFR} bin, and the errorbars show the 16th- and 84th-percentiles. The cyan line shows the best-fit power law between T_{clr} and Σ_{SFR} (equation 17). Bottom panel: ΔT_{clr} (defined in equation 18) displayed as a function of Σ_{SFR} , with a gray line showing zero position.

reference quantity. Quantities that have correlations with T_{clr} stronger than R_g/R_{25} are more likely to have first-order correlations with T_{clr} . Among the quantities with correlation stronger than R_g/R_{25} , Σ_{SFR} has the strongest correlation with T_{clr} ($\rho = 0.89$, showing a strong correlation). This agrees with the baseline assumption in Paper I that the UV radiation from young stars is the dominant dust heating source in the majority of the sample. Σ_{mol} , Σ_{gas} , Σ_{dust} , and Σ_* also have correlations with T_{clr} stronger than R_g/R_{25} . For Σ_{mol} and Σ_{gas} , both correlations likely result from their strong correlations with Σ_{SFR} , i.e. the KS law. The correlation between Σ_* and T_{clr} also likely result from the correlation between Σ_* and Σ_{SFR} , possibly indicating the resolved star-forming main sequence (Cano-Díaz et al. 2016; Abdurro'uf & Akiyama 2017, 2018; Hsieh et al. 2017; Liu et al. 2018; Maragkoudakis et al. 2017; Medling et al. 2018; Lin et al. 2019, 2022; Morselli et al. 2020; Ellison et al. 2021; Pessa

⁸ Paper I adopted $A = 1.0 \pm 0.3 \times 10^{-12}$ and $N = 1.4$.

Table 3. Correlation between ΔT_{clr} and local conditions. We calculate Pearson's correlation coefficient (ρ) along with the p -value of the correlation.

Quantity	Pearson's ρ with ΔT_{clr}	p -value
Σ_{atom}	0.21	$\ll 0.001$
$\log(\Sigma_{\text{mol}})$	-0.12	$\ll 0.001$
$\log(\Sigma_{\text{gas}})$	-0.05	$\ll 0.001$
$\log(\Sigma_{\text{dust}})$	-0.26	$\ll 0.001$
$\log(\text{D/G})$	-0.27	$\ll 0.001$
$\log(\Sigma_{\star})$	0.06	$\ll 0.001$
$12+\log(\text{O/H})$	-0.01	0.012
R_{g}/R_{25}	-0.1	$\ll 0.001$

Notes: (a) ΔT_{clr} is defined in equation (18). (b) Σ_{SFR} is excluded from this table because it has no correlation with ΔT_{clr} , as expected. (c) We consider the correlation as significant when we have $p < 0.05$.

et al. 2022). Σ_{dust} has a correlation slightly stronger than the radial dependence, which might result from its correlation with Σ_{gas} due to the relatively small D/G variations. Note that from the analysis in Paper I, we expect a negative correlation between Σ_{dust} and T_{clr} at fixed Σ_{SFR} because of the effect of dust shielding. We conversely observe a moderately positive correlation between Σ_{dust} and T_{clr} here, since with increasing Σ_{dust} , Σ_{SFR} (or the UV radiation field) increases owing to the KS law.

We display T_{clr} as a function of Σ_{SFR} in the top panel of Fig. 1. As shown in the figure and implied from the correlation, the observed T_{clr} seems to have a power-law dependence on Σ_{SFR} . The best-fit power-law relation is

$$\frac{T_{\text{clr}}}{1 \text{ K}} = (3.50 \pm 0.02) \log \left(\frac{\Sigma_{\text{SFR}}}{1 \text{ M}_{\odot} \text{ yr}^{-1} \text{ kpc}^{-2}} \right) + (28.81 \pm 0.04). \quad (17)$$

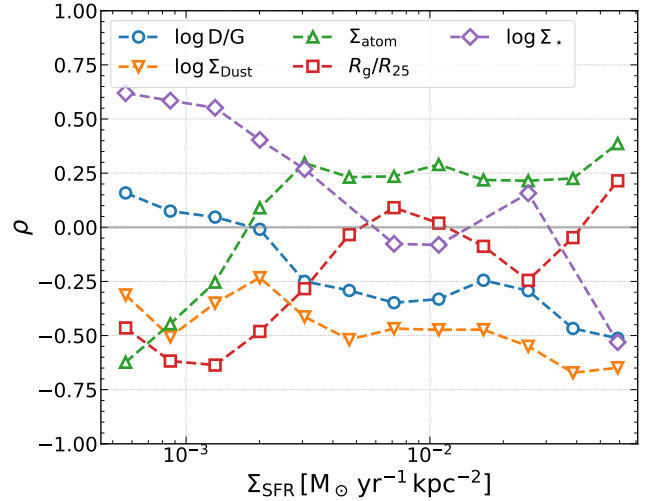
The root-mean-square deviation (RMSD) between measured T_{clr} and the best-fit relation is 0.81 K.⁹ The residual between the measurements and best-fit relation ΔT_{clr} is defined as

$$\Delta T_{\text{clr}} \equiv T_{\text{clr}}^{\text{measured}} - T_{\text{clr}}^{\text{best-fit}}(\Sigma_{\text{SFR}}), \quad (18)$$

where the first and second terms on the right-hand side are the measured and best-fit colour temperatures, respectively. We show ΔT_{clr} as a function of Σ_{SFR} in the bottom panel of Fig. 1. The residual ΔT_{clr} is centred around zero throughout almost the entire observed Σ_{SFR} range, again indicating the significance of the power-law relation between T_{clr} and Σ_{SFR} . However, we do notice that there tends to be a larger scatter toward the low- Σ_{SFR} end, and larger deviation ($> 0.5 \text{ K}$) toward the high- Σ_{SFR} end.

To investigate the possible secondary dependence of T_{clr} on the local environment, we calculate the correlations between ΔT_{clr} and local conditions, and present them in Table 3. All the quantities show weak or no correlations with ΔT_{clr} , indicating that there is no single secondary parameters that strongly affects T_{clr} throughout all observed samples.

To further approach the possible secondary dependence, we group the data points in bins of Σ_{SFR} , and calculate the correlation between ΔT_{clr} and local conditions in each bin. The result is shown in Fig. 2, only keeping the quantities that have their $|\rho| > 0.5$ in at least one of the Σ_{SFR} bins. D/G and Σ_{dust} , which are expected to reduce T_{clr} due to increased opacity from the Paper I analysis, show stronger negative correlations with ΔT_{clr} toward higher Σ_{SFR} . Σ_{dust}

**Figure 2.** Pearson's correlation coefficient (ρ) between ΔT_{clr} (equation 18) and selected local environment quantities in each Σ_{SFR} bin. Quantities made into this selection have their $|\rho|$ values exceeding 0.5 in at least one of the bins. We skip the bins with p -values greater than 0.05, which happens in a few high- Σ_{SFR} bins for $\log \Sigma_{\star}$.

has a stronger correlation than D/G and the correlation coefficient is negative throughout the observed range, suggesting that Σ_{dust} traces the dust opacity effect on T_{clr} more directly in observations than D/G. On the other hand, D/G has a weak but positive correlation coefficient at low Σ_{SFR} , which means that there are other mechanisms that cancel out the opacity effect traced by D/G.

The correlation between ΔT_{clr} and normalized radius is almost a mirror image of the one between ΔT_{clr} and $\log \Sigma_{\star}$, reflecting the fact that the radius normalized by R_{25} correlates with $\log \Sigma_{\star}$, i.e. an exponential disc, in our sample. Similar to the case of D/G mentioned above, the correlation between Σ_{\star} and ΔT_{clr} behaves differently at low and high Σ_{SFR} . Below $\Sigma_{\text{SFR}} \sim 2 \times 10^{-3} \text{ M}_{\odot} \text{ yr}^{-1} \text{ kpc}^{-2}$, Σ_{\star} positively correlates with ΔT_{clr} . This positive correlation for Σ_{\star} might indicate the dust heating contributed by old stellar population in the low- Σ_{SFR} region. At mid- Σ_{SFR} values, Σ_{\star} weakly correlates with ΔT_{clr} . The correlation between Σ_{\star} and ΔT_{clr} jumps to moderately negative strength only at the highest- Σ_{SFR} bin, where the cause is unclear and is to be identified with future data focusing on high Σ_{SFR} regions. The reason for the correlation between ΔT_{clr} and Σ_{atom} is even more difficult to identify because it depends on various complicated factors such as the transition from atomic to molecular phases. Σ_{atom} has a moderately negative correlation with ΔT_{clr} at low Σ_{SFR} , which quickly weakens as Σ_{SFR} increases. At mid- to high- Σ_{SFR} values, Σ_{atom} has a weak positive correlation with ΔT_{clr} .

4.2 Scaling relation between the surface densities of SFR, gas mass, and dust mass

As mentioned in Section 3.4, an underlying assumption in the Paper I model is that at a given D/G, one can infer Σ_{SFR} from Σ_{dust} through the KS law (and Σ_{gas}). Thus, in this subsection, we first present the measured relation between Σ_{SFR} and Σ_{dust} in Fig. 3. As shown in the figure, Σ_{SFR} is correlated with Σ_{dust} . To build a reference for further comparison, we fit a power-law relation between the two. The best-fit

⁹ If we only include pixels with IR measurements $> 3\sigma$ instead of 1σ (Section 2.2), the coefficient, offset and RMSD in equation 17 change to 3.43 ± 0.02 , 28.68 ± 0.05 and 0.80, respectively. These changes are minor compared to the error bars in Fig. 1.

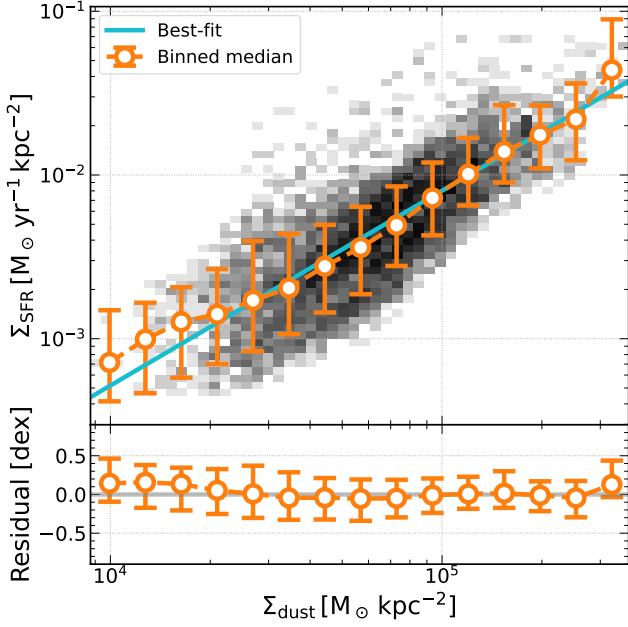


Figure 3. Measured scaling relation between Σ_{SFR} and Σ_{dust} . Top panel: Σ_{SFR} displayed as a function of Σ_{dust} . The gray scale shows the density of data points. The orange circles show the median Σ_{SFR} in each Σ_{dust} bin, and the error bars show the 16th- and 84th-percentiles. The cyan line shows the best-fit power law between Σ_{SFR} and Σ_{dust} . Bottom panel: The residual, $\log(\Sigma_{\text{SFR}}^{\text{measured}}) - \log(\Sigma_{\text{SFR}}^{\text{best-fit}})$ displayed as a function of Σ_{dust} .

relation is:

$$\log\left(\frac{\Sigma_{\text{SFR}}}{1 \text{ M}_{\odot} \text{ yr}^{-1} \text{ kpc}^{-2}}\right) = (1.19 \pm 0.01) \log\left(\frac{\Sigma_{\text{dust}}}{1 \text{ M}_{\odot} \text{ kpc}^{-2}}\right) - (8.05 \pm 0.05). \quad (19)$$

The RMSD of this best-fit relation is 0.27 dex. The residual, $\log(\Sigma_{\text{SFR}}^{\text{measured}}) - \log(\Sigma_{\text{SFR}}^{\text{best-fit}})$, has Pearson's correlation coefficient of -0.36 with D/G , suggesting a medium trend that Σ_{SFR} increases toward regions with lower D/G at a given Σ_{dust} . We compare the measured and best-fit Σ_{SFR} in the top-left panel of Fig. 4. Although we are able to get a solution minimizing the overall RMSD, the solution tends to underestimate Σ_{SFR} at high Σ_{SFR} and overestimate Σ_{SFR} at low Σ_{SFR} . In other words, the $\log(\Sigma_{\text{SFR}}^{\text{best-fit}})$ has a smaller dynamical range than $\log(\Sigma_{\text{SFR}}^{\text{measured}})$.

Inspired by the design of the *Paper I* model, we investigate whether we can improve the prediction of Σ_{SFR} by including D/G as the second variable. This idea is supported by the top-right panel of Fig. 4, where we observe a systematic variation in D/G in the $\log(\Sigma_{\text{SFR}}^{\text{measured}}) - \log(\Sigma_{\text{SFR}}^{\text{best-fit}})$ space. The best-fit Σ_{SFR} in a two-variable (Σ_{dust} , D/G) fitting is

$$\log\left(\frac{\Sigma_{\text{SFR}}}{1 \text{ M}_{\odot} \text{ yr}^{-1} \text{ kpc}^{-2}}\right) = (1.49 \pm 0.01) \log\left(\frac{\Sigma_{\text{dust}}}{1 \text{ M}_{\odot} \text{ kpc}^{-2}}\right) - (0.73 \pm 0.01) \log(D/G) - (11.26 \pm 0.07). \quad (20)$$

The RMSD of this best-fit decreases to 0.22 dex. In the bottom

panels of Fig. 4, we use this fitting to the best-fit Σ_{SFR} ($\Sigma_{\text{SFR}}^{\text{best-fit}}$). We observe that $\Sigma_{\text{SFR}}^{\text{best-fit}}$ now traces the measurements better over the entire observed range, and the systematic trend of D/G in the $\log(\Sigma_{\text{SFR}}^{\text{measured}}) - \log(\Sigma_{\text{SFR}}^{\text{best-fit}})$ space decreases.

With the best-fit result in equation (20), we claim that the assumption in *Paper I*, i.e. scaling of Σ_{SFR} with Σ_{dust} at given D/G , is consistent with our observation. To interpret the equation, we can convert Σ_{dust} in equation (20) to Σ_{gas} and D/G , i.e.

$$\log\left(\frac{\Sigma_{\text{SFR}}}{1 \text{ M}_{\odot} \text{ yr}^{-1} \text{ kpc}^{-2}}\right) \sim 1.49 \log\left(\frac{\Sigma_{\text{gas}}}{1 \text{ M}_{\odot} \text{ kpc}^{-2}}\right) + 0.76 \log(D/G) - 11.26. \quad (21)$$

This functional form could be interpreted as a KS law with a correction term in D/G (hereafter D/G -modified KS law), with higher SFR toward larger D/G at given Σ_{gas} . The 1.49 factor corresponds to the power-law index of KS law (N in equation 16). This is consistent with the $N \sim 1.4$ value measured in *Kennicutt (1998)*; *de los Reyes & Kennicutt (2019)* with total gas; meanwhile, our N value is equal to or steeper than the values measured with molecular-gas-only KS law ($N_{\text{H}_2} \sim 0.8\text{--}1.5$, *Bigiel et al. 2008*; *Blanc et al. 2009*; *Rahman et al. 2011*; *Leroy et al. 2013*; *Kennicutt & De Los Reyes 2021*). The D/G correction term can cause an offset up to ~ 0.8 dex in Σ_{SFR} with the observed D/G range ($\sim 10^{-3}\text{--}10^{-2}$), which is a significant change.

The D/G can influence the star formation activity through the formation of H_2 on dust surfaces (*Krumholz et al. 2008, 2009*; *McKee & Krumholz 2010*). Such a condition may be favourable for star formation through the shielding of UV radiation by H_2 and dust at a given Σ_{gas} . However, it is difficult to prove with our data that the D/G directly affects the star formation activity, because D/G is correlated with various other physical quantities that could affect star formation, such as metallicity, gas pressure, gravitational field, etc. We refer readers who are interested in how these physical quantities could affect SFR to the *Kennicutt & Evans (2012)* review.

5 COMPARING TO THE HIRASHITA & CHIANG (2022) MODEL

5.1 Dependence of T_{clr} on the SFR surface density and D/G

We display both measured and model-predicted T_{clr} as a function of Σ_{SFR} in Fig. 5. The predictions are calculated with the *Paper I* model, the set up descriptions in Section 3.4, and the coefficients in equation (21). From the *Paper I* model, we expect T_{clr} to increase with Σ_{SFR} , and to increase with decreasing D/G at fixed Σ_{SFR} , as shown in the blue and brown lines for $D/G = 1.0 \times 10^{-2}$ and 2.0×10^{-3} , respectively. To compare with this prediction, we select data points within ± 0.1 dex of the two desired D/G values and plot them with connected data points with error bars in Fig. 5.

We observe that both the $D/G \sim 1.0 \times 10^{-2}$ and $D/G \sim 2.0 \times 10^{-3}$ groups follow the predicted trend at $\Sigma_{\text{SFR}} \gtrsim 10^{-2} \text{ M}_{\odot} \text{ yr}^{-1} \text{ kpc}^{-2}$. Meanwhile, the separation of the two observed trends is not significant, with both groups falling within the 1σ scatter of data points of each other. At lower Σ_{SFR} , the observed T_{clr} exceeds the model prediction. Moreover, the difference in T_{clr} between different D/G values become even less distinguishable. This implies that some assumptions made in *Paper I* might break down at low Σ_{SFR} as we will discuss in Section 5.3. Nevertheless, we emphasize that the *Paper I*

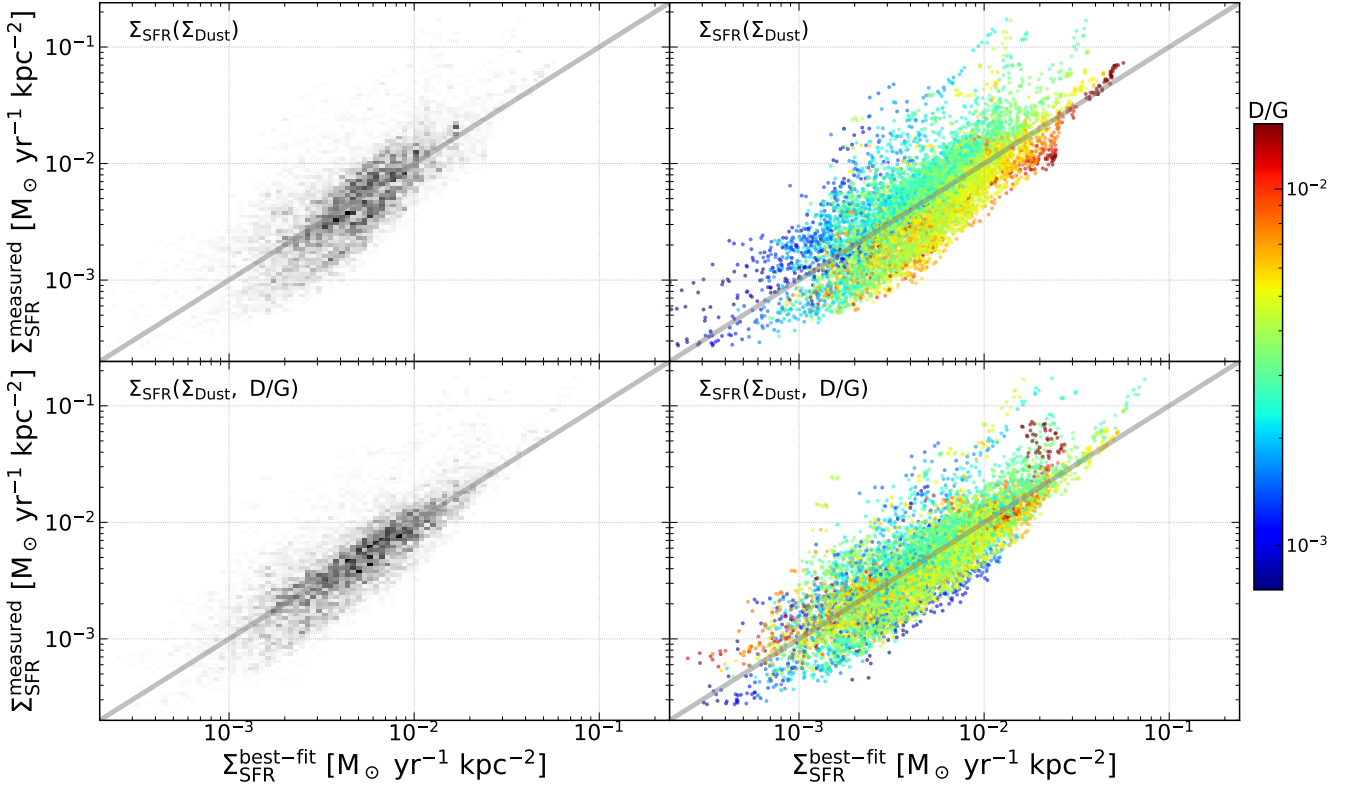


Figure 4. Comparison between measured Σ_{SFR} ($\Sigma_{\text{SFR}}^{\text{measured}}$) and Σ_{SFR} predicted from best-fit relations ($\Sigma_{\text{SFR}}^{\text{best-fit}}$) with Σ_{dust} alone (top panels) or with both Σ_{dust} and D/G (bottom panels). The left panels have their transparency indicating the distribution of data points, while the right panel shows the pixel-by-pixel data points colored by D/G.

model reproduces not only the overall trend but also the different relations for different values of D/G at $\Sigma_{\text{SFR}} \gtrsim 10^{-2} \text{ M}_{\odot} \text{ yr}^{-1} \text{ kpc}^{-2}$.

5.2 Dependence of T_{clr} on the surface densities of SFR and dust

One interesting conclusion in [Paper I](#) is that with Σ_{SFR} and Σ_{dust} , one will be able to determine dust temperature (details in their Section 3.3). To test this with our data, we calculate T_{clr} from the measured Σ_{SFR} and Σ_{dust} in this work with the [Paper I](#) model, and compare the model-predicted T_{clr} to the measured one (the predicted data thus do not have matching Σ_{gas} and D/G with observations). As shown in Fig. 6, the measured T_{clr} ($T_{\text{clr}}^{\text{measured}}$) and model-predicted T_{clr} ($T_{\text{clr}}^{\text{model}}$) trace each other, with RMSD = 1.6 K. However, $T_{\text{clr}}^{\text{measured}}$ has a smaller dynamic range than $T_{\text{clr}}^{\text{model}}$. At $T_{\text{clr}} \lesssim (\gtrsim) 22.5 \text{ K}$, the model tends to underestimate (overestimate) T_{clr} . The difference at the highest-temperature end is possibly due to the scatter resulting from lack of measurements: although we have ~ 16 per cent of data points with $T_{\text{clr}}^{\text{measured}} > 22.5 \text{ K}$, only ~ 2 per cent of the data have $T_{\text{clr}}^{\text{measured}} > 25 \text{ K}$. As mentioned in Section 4.1, a larger sample focusing on high Σ_{SFR} (i.e. high T_{clr}) is necessary to draw a firm conclusion for the dust properties at the high- T_{clr} end. The difference in the low-temperature part connects back to the underestimation of T_{clr} in low- Σ_{SFR} regions described in Section 5.1. As shown in the left panel of Fig. 6, the threshold below which the model underestimates T_{clr} is near $\Sigma_{\text{SFR}} \sim 10^{-2} \text{ M}_{\odot} \text{ yr}^{-1} \text{ kpc}^{-2}$, the same threshold we found in Section 5.1. The $T_{\text{clr}}^{\text{model}}$ has a correlation coefficient of 0.97 with $\log \Sigma_{\text{SFR}}$, ~ 0.09 higher than the one of $T_{\text{clr}}^{\text{measured}}$, indicating a slight overestimation of the role of Σ_{SFR} in

dust heating in the model. On the other hand, $T_{\text{clr}}^{\text{model}}$ has a correlation coefficient of 0.67 with $\log \Sigma_{\text{dust}}$, ~ 0.06 higher than the one with $T_{\text{clr}}^{\text{measured}}$, indicating a possible underestimation of the strength of dust shielding.

5.3 Implications for the Hirashita & Chiang (2022) model

Through the various comparisons, we found that the analytical model proposed in [Paper I](#) successfully reproduced the first-order dependence of T_{clr} on Σ_{SFR} . The predicted T_{clr} has correlation coefficients with Σ_{SFR} and Σ_{dust} quite similar to the observations. The predicted T_{clr} from Σ_{SFR} and Σ_{dust} traces the observed T_{clr} , with a RMSD of 1.6 K.

The prediction of higher T_{clr} toward lower D/G at fixed Σ_{SFR} is less obvious in the observations. The phenomena are only seen above $\Sigma_{\text{SFR}} \sim 10^{-2} \text{ M}_{\odot} \text{ yr}^{-1} \text{ kpc}^{-2}$ (or $T_{\text{clr}} \sim 22.5 \text{ K}$; Fig. 5). Below that, the model tends to underestimate T_{clr} , and the observed T_{clr} is not sensitive to D/G at fixed Σ_{SFR} . This suggests that there are physical mechanisms not modeled in the low- Σ_{SFR} region, which will be discussed below. However, this caveat will likely not affect the high-redshift applications, which the model was originally designed for, as high-redshift targets usually have Σ_{SFR} higher than the sample in this paper.

We raise three possible explanations for the higher observed temperature at low- Σ_{SFR} . The first possibility is that the contribution to dust heating from old stars might be more important than assumed in the [Paper I](#) model ([Groves et al. 2012](#); [De Looze et al. 2014](#); [Nersisyan et al. 2019](#)). For instance, [Abdurro'uf et al. \(2022b\)](#) showed, using a spatially resolved analysis of nearby galaxies, that the en-

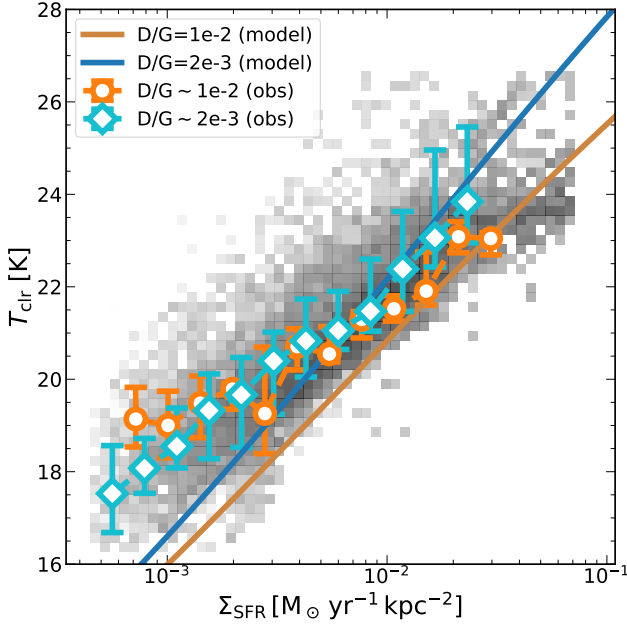


Figure 5. Comparison between the predicted and measured relations between T_{dust} and Σ_{SFR} . The solid lines show the predicted T_{dust} at two D/G values ($D/G = 1.0 \times 10^{-2}$ and 2.0×10^{-3} for brown and blue lines, respectively) from the [Paper I](#) model, calculated with coefficients in equation (21). The data points with error bars present the measured T_{dust} within ± 0.1 dex of the desired D/G values (1.0×10^{-2} and 2.0×10^{-3} for orange and cyan, respectively). The gray colour shows the distribution of all measurements (the same one shown in Fig. 1).

ergy contribution from old stars to dust heating increases as sSFR decreases (see also [Boquien et al. 2016](#); [Leja et al. 2019](#)). In Fig. 7, we show the measured sSFR as a function of Σ_{SFR} . We observe that the sSFR becomes lower towards lower Σ_{SFR} . This trend means that the fraction of young stars is up to three times lower comparing to old stars, not emitting UV radiation, at the lowest Σ_{SFR} bin. This observation suggests that the assumption of young-star-dominated heating is only applicable above certain threshold of Σ_{SFR} , which is around $\Sigma_{\text{SFR}} \sim 1 \times 10^{-2} \text{ M}_{\odot} \text{ yr}^{-1} \text{ kpc}^{-2}$.

The second explanation is the difference in the stellar ages set by the model and traced by observations. In the model, we assume that the SFR is constant over the past $\tau_{\star} = 10^{10}$ yr. However, our FUV and IR indicators only trace stars with age up to $\sim 10^8$ yr (see [Kennicutt & Evans 2012](#), and references therein). If the SFR at age $> 10^8$ yr is higher than the current SFR (e.g. the decaying SFR in [Nersesian et al. 2019](#)), the constant-SFR model would underestimate the dust heating contributed from old ($> 10^8$ yr) stellar populations and thus the dust temperature.

The above two possibilities can be tested by adding a stellar SED of an old stellar population to the [Paper I](#) model. For the purpose of this test, we add a stellar SED generated by `STARBURST99` with an instantaneous burst occurring 1 Gyr ago, which is old enough not to contribute to the observed SFR, but young enough to contribute significantly to the dust temperature. Moreover, we choose the total stellar mass formed by this instantaneous burst two times larger than the original component (formed by a constant SFR over time), so that the sSFR is roughly three times lower. As a consequence, the dust temperature at $\Sigma_{\text{SFR}} = 10^{-3} \text{ M}_{\odot} \text{ yr}^{-1} \text{ kpc}^{-2}$ is raised to 18 and 19 K for $D/G = 10^{-2}$ and 2×10^{-3} , respectively (originally ~ 16 K). These

temperatures are consistent with the observed values, thus supporting the contribution from old stellar population as a reason for the higher dust temperatures in the observations than in the [Paper I](#) model. Since the old stellar population contributes to emission at longer wavelengths, its emission is less affected by dust extinction. This may also explain the small difference between the two cases of D/G values at low Σ_{SFR} .

The third explanation we bring up is the spatial distribution of dust. In the [Paper I](#) model, we assume a uniform distribution of dust and stars in the plane of the galaxy disc, and adopt a thin-disc approximation. However, it is possible that in the outer disc, dust is less localized with young stars. This is supported by the residual shown in Fig. 3: in the low- Σ_{SFR} region, the observation deviates toward higher Σ_{SFR} per Σ_{dust} , in other words, lower Σ_{dust} at fixed Σ_{SFR} . This trend effectively lowers down the dust opacity and could raise the dust temperature. [Alton et al. \(1998\)](#), [Bianchi \(2007\)](#), [Muñoz-Mateos et al. \(2009a\)](#) and [Hunt et al. \(2015a\)](#) also showed that the exponential scale length of dust is longer (more extensive) than the one of stars. However, we remind the readers that there are also literature showing consistent spatial distribution between dust and FUV, e.g. [Casasola et al. \(2017\)](#) showed that Σ_{dust} and I_{FUV} have almost identical mean scale lengths ($h \sim 0.4R_{25}$) in the DustPedia sample.

6 SUMMARY

In this work, we investigate the spatially resolved properties of dust temperature in nearby galaxies. We examine how the dust temperature is regulated by the surface densities of various quantities such as Σ_{SFR} , Σ_{dust} , and Σ_{gas} , with both observations and model predictions. To achieve this goal, we compile multi-wavelength observations of dust, stars and SFR in 46 nearby galaxies, and make a 2 kpc scale map of each component. We measure how dust temperature (the 250 μm -to-100 μm colour temperature) scales with local physical conditions, and then compare our measurements to the dust temperature model developed by [Paper I](#). We find the following features for the measured dust properties:

- The measured T_{dust} correlates well with spatially resolved Σ_{SFR} . The best-fit power law yields a RMSD of 0.81 K.
- None of the measured quantities has an overall strong correlation with the residual of the above power-law fitting, ΔT_{dust} . When analyzed in each Σ_{SFR} bin, we find some trends: Both D/G and Σ_{dust} have stronger negative correlations with ΔT_{dust} at mid to high Σ_{SFR} , meaning that the effect of lower T_{dust} due to increased dust opacity is stronger at high- Σ_{SFR} regions.
- We provide an empirical formula to predict Σ_{SFR} with Σ_{dust} and D/G (equation 20). This is equivalent to a KS law modified by a secondary dependence on D/G.

Here is the summary of our key findings by comparing the measured dust temperature to the one predicted with the [Paper I](#) analytical dust temperature model:

- Our observations show that T_{dust} strongly correlates with Σ_{SFR} and that at fixed Σ_{SFR} , T_{dust} increases as D/G decreases at $\Sigma_{\text{SFR}} \gtrsim 1.0 \times 10^{-2} \text{ M}_{\odot} \text{ yr}^{-1} \text{ kpc}^{-2}$. These results are consistent with the [Paper I](#) model. The latter is interpreted as less dust shielding in a dust-poor environment.
- The T_{dust} predicted from Σ_{SFR} and Σ_{dust} by the [Paper I](#) model using the newly derived star formation relation is reasonably consistent with observations, with a RMSD of 1.6 K. However, we observe a weaker dependence of T_{dust} on Σ_{SFR} with our measurements.

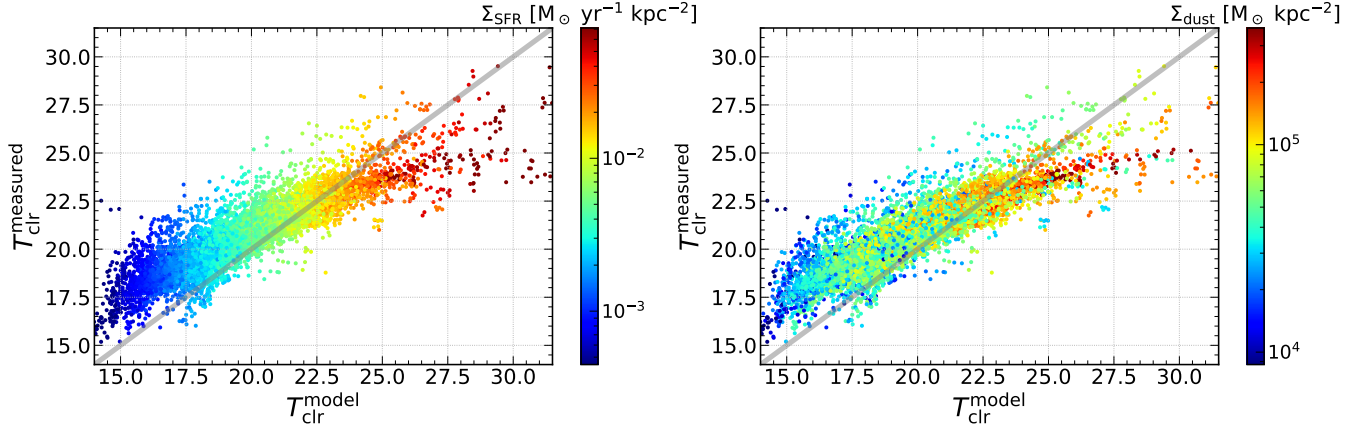


Figure 6. Measured and model-predicted T_{clr} . The latter quantity, $T_{\text{clr}}^{\text{model}}$, is calculated with the measured pixel-by-pixel $(\Sigma_{\text{SFR}}, \Sigma_{\text{dust}})$ pair using the star formation law described in equation (21). The same data are plotted in the left and right panels, of which the data points are colour-coded by Σ_{SFR} and Σ_{dust} , respectively.

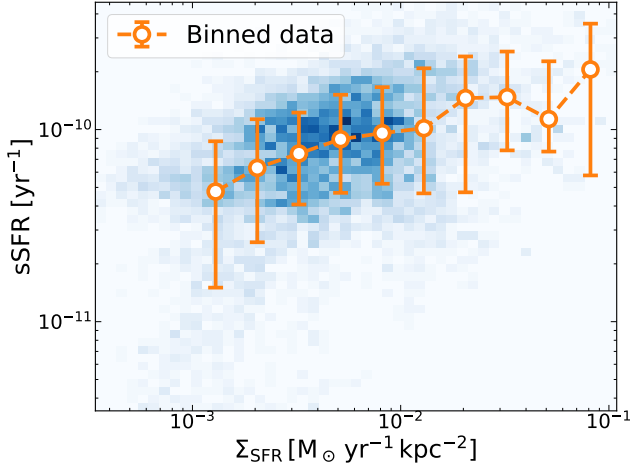


Figure 7. Relation between sSFR and Σ_{SFR} in our sample. The points connected by the dashed line show the median of sSFR in each Σ_{SFR} bin with the error bar showing the standard deviation, and the blue colour level shows the density of the pixel-by-pixel measurements on this diagram.

- At low Σ_{SFR} ($\lesssim 10^{-2} \text{ M}_{\odot} \text{ yr}^{-1} \text{ kpc}^{-2}$), our observed T_{clr} is higher than the prediction from the [Paper I](#) model, and it has no significant dependence on D/G. This is likely due to the contribution of dust heating from old stellar population and/or the variation of SFR within the past 10^{10} yr.

We conclude that the dust temperature reasonably scales with Σ_{SFR} . At high- Σ_{SFR} , the T_{clr} at fixed Σ_{SFR} decreases as D/G increases, which means that the [Paper I](#) model is consistent with observations at $\Sigma_{\text{SFR}} \gtrsim 10^{-2} \text{ M}_{\odot} \text{ yr}^{-1} \text{ kpc}^{-2}$. Thus, we confirm that dust heating from young stars and shielding of radiation by dust regulate the dust temperature. We also propose a prescription to predict Σ_{SFR} from Σ_{gas} and D/G, i.e. a D/G-modified KS law. In the end, we succeed in obtaining a comprehensive understanding for the relations among dust temperature, dust content and star formation activity.

ACKNOWLEDGEMENTS

We thank the anonymous referee for useful comments that helped to improve the quality of the manuscript. IC thanks E. Schinnerer for useful discussions about this work. IC and HH thank the National Science and Technology Council for support through grants 108-2112-M-001-007-MY3 and 111-2112-M-001-038-MY3, and the Academia Sinica for Investigator Award AS-IA-109-M02. AS is supported by an NSF Astronomy and Astrophysics Postdoctoral Fellowship under award AST-1903834. EWK acknowledges support from the Smithsonian Institution as a Submillimeter Array (SMA) Fellow and the Natural Sciences and Engineering Research Council of Canada (NSERC). JS acknowledges support by NSERC through a Canadian Institute for Theoretical Astrophysics (CITA) National Fellowship.

This work uses observations made with ESA *Herschel* Space Observatory. *Herschel* is an ESA space observatory with science instruments provided by European-led Principal Investigator consortia and with important participation from NASA.

This paper makes use of the VLA data with project codes 14A-468, 14B-396, 16A-275 and 17A-073, which has been processed as part of the EveryTHINGS survey. This paper makes use of the VLA data with legacy ID AU157, which has been processed in the PHANGS-VLA survey. The National Radio Astronomy Observatory is a facility of the National Science Foundation operated under cooperative agreement by Associated Universities, Inc. This publication makes use of data products from the Wide-field Infrared Survey Explorer, which is a joint project of the University of California, Los Angeles, and the Jet Propulsion Laboratory/California Institute of Technology, funded by the National Aeronautics and Space Administration.

This paper makes use of the following ALMA data, which have been processed as part of the PHANGS-ALMA CO(2–1) survey: ADS/JAO.ALMA#2012.1.00650.S, ADS/JAO.ALMA#2015.1.00782.S, ADS/JAO.ALMA#2018.1.01321.S, ADS/JAO.ALMA#2018.1.01651.S.

ALMA is a partnership of ESO (representing its member states), NSF (USA) and NINS (Japan), together with NRC (Canada), MOST and ASIAA (Taiwan), and KASI (Republic of Korea),

in cooperation with the Republic of Chile. The Joint ALMA Observatory is operated by ESO, AUI/NRAO and NAOJ.

This research made use of Astropy,¹⁰ a community-developed core Python package for Astronomy ([Astropy Collaboration et al. 2013, 2018, 2022](#)). This research has made use of NASA's Astrophysics Data System Bibliographic Services. We acknowledge the usage of the HyperLeda database (<http://leda.univ-lyon1.fr>). This research has made use of the NASA/IPAC Extragalactic Database (NED), which is funded by the National Aeronautics and Space Administration and operated by the California Institute of Technology.

DATA AVAILABILITY

Data related to this publication and its figures are available on reasonable request from the corresponding author.

REFERENCES

- Abdo A. A., et al., 2010, *ApJ*, **710**, 133
- Abdurro'uf Akiyama M., 2017, *MNRAS*, **469**, 2806
- Abdurro'uf Akiyama M., 2018, *MNRAS*, **479**, 5083
- Abdurro'uf et al., 2022a, *ApJS*, **259**, 35
- Abdurro'uf Lin Y.-T., Hirashita H., Morishita T., Tacchella S., Akiyama M., Takeuchi T. T., Wu P.-F., 2022b, *ApJ*, **926**, 81
- Accurso G., et al., 2017, *MNRAS*, **470**, 4750
- Alton P. B., et al., 1998, *A&A*, **335**, 807
- Aniano G., Draine B. T., Gordon K. D., Sandstrom K., 2011, *PASP*, **123**, 1218
- Aniano G., et al., 2012, *ApJ*, **756**, 138
- Aniano G., et al., 2020, *ApJ*, **889**, 150
- Asplund M., Grevesse N., Sauval A. J., Scott P., 2009, *ARA&A*, **47**, 481
- Astropy Collaboration et al., 2013, *A&A*, **558**, A33
- Astropy Collaboration et al., 2018, *AJ*, **156**, 123
- Astropy Collaboration et al., 2022, *ApJ*, **935**, 167
- Bakx T. J. L. C., et al., 2021, *MNRAS*, **508**, L58
- Barrera-Ballesteros J. K., et al., 2016, *MNRAS*, **463**, 2513
- Barrera-Ballesteros J. K., et al., 2021, *MNRAS*, **503**, 3643
- Bendo G. J., et al., 2012, *MNRAS*, **419**, 1833
- Bendo G. J., et al., 2015, *MNRAS*, **448**, 135
- Bernstein R. A., Freedman W. L., Madore B. F., 2002, *ApJ*, **571**, 56
- Bianchi S., 2007, *A&A*, **471**, 765
- Bianchi S., et al., 2018, *A&A*, **620**, A112
- Bigiel F., Leroy A., Walter F., Brinks E., de Blok W. J. G., Madore B., Thornley M. D., 2008, *AJ*, **136**, 2846
- Blanc G. A., Heiderman A., Gebhardt K., Evans Neal J. I., Adams J., 2009, *ApJ*, **704**, 842
- Bolatto A. D., Wolfire M., Leroy A. K., 2013, *ARA&A*, **51**, 207
- Boquien M., et al., 2016, *A&A*, **591**, A6
- Bouwens R. J., et al., 2016, *ApJ*, **833**, 72
- Braun R., Thilker D. A., Walterbos R. A. M., Corbelli E., 2009, *ApJ*, **695**, 937
- Buat V., et al., 2005, *ApJ*, **619**, L51
- Buat V., et al., 2012, *A&A*, **545**, A141
- Burgarella D., Nanni A., Hirashita H., Theulé P., Inoue A. K., Takeuchi T. T., 2020, *A&A*, **637**, A32
- Calzetti D., 2001, *PASP*, **113**, 1449
- Cano-Díaz M., et al., 2016, *ApJ*, **821**, L26
- Capak P. L., et al., 2015, *Nature*, **522**, 455
- Casasola V., et al., 2017, *A&A*, **605**, A18
- Casasola V., et al., 2022, *A&A*, **668**, A130
- Cazaux S., Tielens A. G. G. M., 2004, *ApJ*, **604**, 222
- Chastenot J., et al., 2021, *ApJ*, **912**, 103
- Chiang I.-D., 2021, PhD thesis, University of California San Diego
- Chiang I.-D., Sandstrom K. M., Chastenot J., Johnson L. C., Leroy A. K., Utomo D., 2018, *ApJ*, **865**, 117
- Chiang I.-D., et al., 2021, *ApJ*, **907**, 29
- Compiègne M., et al., 2011, *A&A*, **525**, A103
- Corbelli E., Lorenzoni S., Walterbos R., Braun R., Thilker D., 2010, *A&A*, **511**, A89
- Dale D. A., Helou G., Contursi A., Silbermann N. A., Kolhatkar S., 2001, *ApJ*, **549**, 215
- Dale D. A., et al., 2012, *ApJ*, **745**, 95
- Davies J. I., et al., 2017, *PASP*, **129**, 044102
- De Looze I., et al., 2014, *A&A*, **571**, A69
- de Blok W. J. G., Walter F., Brinks E., Trachternach C., Oh S.-H., Kennicutt R. C., 2008, *AJ*, **136**, 2648
- Desert F.-X., Boulanger F., Puget J. L., 1990, *A&A*, **237**, 215
- Draine B. T., 2003, *ApJ*, **598**, 1017
- Draine B. T., Li A., 2007, *ApJ*, **657**, 810
- Draine B. T., et al., 2014, *ApJ*, **780**, 172
- Druard C., et al., 2014, *A&A*, **567**, A118
- Ellison S. L., Lin L., Thorp M. D., Pan H.-A., Scudder J. M., Sánchez S. F., Bluck A. F. L., Maiolino R., 2021, *MNRAS*, **501**, 4777
- Emsellem E., et al., 2022, *A&A*, **659**, A191
- Enia A., et al., 2020, *MNRAS*, **493**, 4107
- Faesi C. M., Lada C. J., Forbrich J., Menten K. M., Bouy H., 2014, *ApJ*, **789**, 81
- Ferrara A., et al., 2022, *MNRAS*, **512**, 58
- Galliano F., Galametz M., Jones A. P., 2018, *ARA&A*, **56**, 673
- Glover S. C. O., Mac Low M. M., 2011, *MNRAS*, **412**, 337
- Gordon K. D., et al., 2014, *ApJ*, **797**, 85
- Gould R. J., Salpeter E. E., 1963, *ApJ*, **138**, 393
- Gratier P., et al., 2010, *A&A*, **522**, A3
- Griffin M. J., et al., 2010, *A&A*, **518**, L3
- Groves B., et al., 2012, *MNRAS*, **426**, 892
- Heald G., et al., 2011, *A&A*, **526**, A118
- Hensley B. S., Draine B. T., 2022, arXiv e-prints, p. arXiv:2208.12365
- Hildebrand R. H., 1983, *QJRAS*, **24**, 267
- Hirashita H., Chiang I. D., 2022, *MNRAS*, **516**, 1612
- Hsieh B. C., et al., 2017, *ApJ*, **851**, L24
- Hunt L. K., et al., 2015a, *A&A*, **576**, A33
- Hunt L. K., et al., 2015b, *A&A*, **583**, A114
- Jenkins E. B., 2009, *ApJ*, **700**, 1299
- Jones A. P., Köhler M., Ysard N., Bocchio M., Verstraete L., 2017, *A&A*, **602**, A46
- Kennicutt Robert C. J., 1998, *ApJ*, **498**, 541
- Kennicutt Robert C. J., De Los Reyes M. A. C., 2021, *ApJ*, **908**, 61
- Kennicutt R. C., Evans N. J., 2012, *ARA&A*, **50**, 531
- Koch E. W., et al., 2018, *MNRAS*, **479**, 2505
- Krumholz M. R., McKee C. F., Tumlinson J., 2008, *ApJ*, **689**, 865
- Krumholz M. R., McKee C. F., Tumlinson J., 2009, *ApJ*, **693**, 216
- Kuno N., et al., 2007, *PASJ*, **59**, 117
- Lang P., et al., 2020, *ApJ*, **897**, 122
- Leitherer C., et al., 1999, *ApJS*, **123**, 3
- Leja J., et al., 2019, *ApJ*, **877**, 140
- Leroy A. K., et al., 2009, *AJ*, **137**, 4670
- Leroy A. K., et al., 2011, *ApJ*, **737**, 12
- Leroy A. K., et al., 2013, *AJ*, **146**, 19
- Leroy A. K., et al., 2019, *ApJS*, **244**, 24
- Leroy A. K., et al., 2021a, *ApJS*, **255**, 19
- Leroy A. K., et al., 2021b, *ApJS*, **257**, 43
- Leroy A. K., et al., 2022, *ApJ*, **927**, 149
- Lin L., et al., 2019, *ApJ*, **884**, L33
- Lin L., et al., 2022, *ApJ*, **926**, 175
- Liu Q., Wang E., Lin Z., Gao Y., Liu H., Berhane Teklu B., Kong X., 2018, *ApJ*, **857**, 17
- Liu D., et al., 2019, *ApJS*, **244**, 40
- Makarov D., Prugniel P., Terekhova N., Courtois H., Vauglin I., 2014, *A&A*, **570**, A13

¹⁰ <http://www.astropy.org>

Maragkoudakis A., Zezas A., Ashby M. L. N., Willner S. P., 2017, *MNRAS*, **466**, 1192

Martin D. C., et al., 2005, *ApJ*, **619**, L1

Mathis J. S., Mezger P. G., Panagia N., 1983, *A&A*, **128**, 212

McCormick A., Veilleux S., Rupke D. S. N., 2013, *ApJ*, **774**, 126

McKee C. F., Krumholz M. R., 2010, *ApJ*, **709**, 308

Medling A. M., et al., 2018, *MNRAS*, **475**, 5194

Meidt S. E., Rand R. J., Merrifield M. R., 2009, *ApJ*, **702**, 277

Morselli L., et al., 2020, *MNRAS*, **496**, 4606

Moustakas J., et al., 2011, arXiv e-prints, p. arXiv:1112.3300

Muñoz-Mateos J. C., et al., 2009a, *ApJ*, **701**, 1965

Muñoz-Mateos J. C., et al., 2009b, *ApJ*, **703**, 1569

Nersesian A., et al., 2019, *A&A*, **624**, A80

Nersesian A., et al., 2021, *MNRAS*, **506**, 3986

Nieten C., Neininger N., Guélin M., Ungerechts H., Lucas R., Berkhuijsen E. M., Beck R., Wielebinski R., 2006, *A&A*, **453**, 459

Peimbert A., Peimbert M., 2010, *ApJ*, **724**, 791

Pessa I., et al., 2022, *A&A*, **663**, A61

Pilbratt G. L., et al., 2010, *A&A*, **518**, L1

Pilyugin L. S., Grebel E. K., 2016, *MNRAS*, **457**, 3678

Poglitsch A., et al., 2010, *A&A*, **518**, L2

Puche D., Carignan C., van Gorkom J. H., 1991, *AJ*, **101**, 456

Rahman N., et al., 2011, *ApJ*, **730**, 72

Relaño M., Lisenfeld U., Hou K. C., De Looze I., Vílchez J. M., Kennicutt R. C., 2020, *A&A*, **636**, A18

Roussel H., 2013, *PASP*, **125**, 1126

Salim S., et al., 2016, *ApJS*, **227**, 2

Salim S., Boquien M., Lee J. C., 2018, *ApJ*, **859**, 11

Sánchez S. F., et al., 2013, *A&A*, **554**, A58

Sánchez S. F., et al., 2014, *A&A*, **563**, A49

Sánchez S. F., et al., 2019, *MNRAS*, **484**, 3042

Sánchez S. F., et al., 2021, *MNRAS*, **503**, 1615

Sandstrom K. M., et al., 2013, *ApJ*, **777**, 5

Santoro F., et al., 2022, *A&A*, **658**, A188

Schruba A., et al., 2011, *AJ*, **142**, 37

Schruba A., et al., 2012, *AJ*, **143**, 138

Schwartz P. R., 1982, *ApJ*, **252**, 589

Smith M. W. L., et al., 2012, *ApJ*, **756**, 40

Sofue Y., Tutui Y., Honma M., Tomita A., Takamiya T., Koda J., Takeda Y., 1999, *ApJ*, **523**, 136

Solomon P. M., Rivolo A. R., Barrett J., Yahil A., 1987, *ApJ*, **319**, 730

Sommovigo L., et al., 2022, *MNRAS*, **513**, 3122

Sorai K., et al., 2019, *PASJ*, **71**, S14

Strong A. W., Mattox J. R., 1996, *A&A*, **308**, L21

Sun J., et al., 2020, *ApJ*, **892**, 148

Sun J., et al., 2022, *AJ*, **164**, 43

Tabatabaei F. S., et al., 2014, *A&A*, **561**, A95

Tully R. B., Rizzi L., Shaya E. J., Courtois H. M., Makarov D. I., Jacobs B. A., 2009, *AJ*, **138**, 323

Utomo D., Chiang I.-D., Leroy A. K., Sandstrom K. M., Chasteney J., 2019, *ApJ*, **874**, 141

Vílchez J. M., Relaño M., Kennicutt R., De Looze I., Mollá M., Galametz M., 2019, *MNRAS*, **483**, 4968

Walter F., Brinks E., de Blok W. J. G., Bigiel F., Kennicutt Jr. R. C., Thornley M. D., Leroy A., 2008, *AJ*, **136**, 2563

Watson D., Christensen L., Knudsen K. K., Richard J., Gallazzi A., Michałowski M. J., 2015, *Nature*, **519**, 327

Wolfire M. G., Hollenbach D., McKee C. F., 2010, *ApJ*, **716**, 1191

Wright E. L., et al., 2010, *AJ*, **140**, 1868

Yamasawa D., Habe A., Kozasa T., Nozawa T., Hirashita H., Umeda H., Nomoto K., 2011, *ApJ*, **735**, 44

Zurita A., Florido E., Bresolin F., Pérez-Montero E., Pérez I., 2021, *MNRAS*, **500**, 2359

de los Reyes M. A. C., Kennicutt Robert C. J., 2019, *ApJ*, **872**, 16

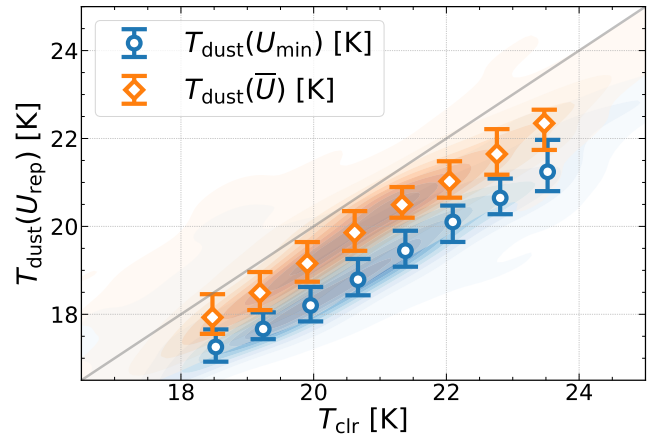


Figure A1. Comparison between the dust temperature tracers. The horizontal axis shows T_{clr} , the FIR-based single dust temperature. The vertical axis presents $T_{\text{dust}}(U_{\text{rep}})$, the effective temperature converted from the ISRF distribution function. The blue shades show the density plot of pixel-by-pixel measurements of $T_{\text{dust}}(U_{\text{min}})$, and the blue line shows the median in each T_{clr} bin. The orange shades and line show the counterparts for $T_{\text{dust}}(\bar{U})$.

APPENDIX A: CONSISTENCY BETWEEN DUST TEMPERATURE TRACERS

In our analysis, we use T_{clr} as the fiducial tracer for dust temperature. There are other commonly used tracers for dust temperature that can be derived from dust SED fitting. Broadly, there are two different approaches: (1) the single temperature derived from the modified blackbody model (Schwartz 1982; Hildebrand 1983), which focuses on the emission in the FIR from large grains in radiative equilibrium and (2) the effective temperature derived from the distribution function of ISRF, which is a product of SED fitting with a physical dust model (e.g. Dale et al. 2001; Draine & Li 2007). The latter usually includes the non-equilibrium thermal emission from small grains. In this section, we briefly examine the consistency between these two approaches, i.e. the colour temperature (T_{clr}) introduced in the main text, which focuses on the equilibrium emission in the FIR thus belongs to the first approach, and the ISRF strength from SED fitting results in τOMGS (J. Chasteney et al. in preparation, fitting done with the Draine & Li 2007, model), which belongs to the second method.

In the Draine & Li (2007) model, the scaled ISRF intensity is denoted as U , expressed in units of the MW diffuse ISRF at 10 kpc from Mathis et al. (1983). The ISRF contributing to dust heating is described by a combination of two components: a fraction of dust mass (γ) heated by a power-law distribution ($\propto U^{-\alpha}$) of starlight with $U_{\text{min}} \leq U \leq U_{\text{max}}$ (Dale et al. 2001), and the rest $(1 - \gamma)$ of dust mass heated by $U = U_{\text{min}}$, i.e. diffuse ISM radiation.

J. Chasteney et al. (in preparation) fix $\alpha = 2$ and $U_{\text{max}} = 10^7$, and leaves γ and U_{min} as free parameters (following Aniano et al. 2012, 2020). According to Draine et al. (2014), we can convert a representative ISRF (U_{rep}) to a representative dust temperature with:

$$\frac{T_{\text{dust}}(U_{\text{rep}})}{1 \text{ K}} = 18 \times U_{\text{rep}}^{1/6}. \quad (\text{A1})$$

There are two commonly used conventions for U_{rep} . One is $U_{\text{rep}} = U_{\text{min}}$ by assuming that the majority of dust mass is heated by U_{min} , i.e. $\gamma \ll 1$. This assumption is true almost throughout the entire M101 (Chasteney et al. 2021) and regions with high dust luminosity surface density (Aniano et al. 2012; Chasteney et al. 2021). The other convention adopts the dust-mass-averaged ISRF, \bar{U} , as U_{rep} . The

functional form of \bar{U} is:

$$\bar{U} = (1 - \gamma)U_{\min} + \gamma U_{\min} \frac{\ln(U_{\max}/U_{\min})}{1 - (U_{\min}/U_{\max})} \quad \text{for } \alpha = 2. \quad (\text{A2})$$

With that said, the three T_{dust} tracers we will compare here are: T_{clr} , $T_{\text{dust}}(U_{\min})$ and $T_{\text{dust}}(\bar{U})$ (equations 3, A1 and A2). As shown in Fig. A1, the three tracers are roughly parallel to each other in the temperature range of interest, suggesting that these temperature tracers reasonably trace each other with a possible systematic offset in the calibration between T_{clr} and the representative T_{dust} converted from the ISRF strength. T_{clr} is systematically ~ 0.8 K and ~ 1.8 K higher than $T_{\text{dust}}(\bar{U})$ and $T_{\text{dust}}(U_{\min})$, respectively. The fact that $T_{\text{dust}}(\bar{U})$ is consistently higher than $T_{\text{dust}}(U_{\min})$ suggests that the hotter dust component, which is represented by the power-law component in the Draine & Li (2007) formulation, is important in the model. The ~ 0.4 K ($\sim 2\%$ in T_{dust} , or ~ 0.05 dex in U) offset between T_{clr} and $T_{\text{dust}}(\bar{U})$ is roughly 2.5 times the typical uncertainty in \bar{U} from J. Chastenot et al. (in preparation, $\sigma \sim 0.02$ dex), which indicates that this offset is significant.

APPENDIX B: ROBUSTNESS UNDER THE ADOPTED CO-TO-H₂ CONVERSION FACTORS

As we mentioned in Section 3.2, how the CO-to-H₂ conversion factor, α_{CO} , depends on local conditions is still an active field of study. In our main analysis, we calculate α_{CO} with the prescription suggested by Bolatto et al. (2013), because it is one of the few prescriptions that formulate both the CO-dark molecular gas and the decrease of α_{CO} in galaxy centres, where the latter has been proved to be necessary to obtain reasonable values for D/G and D/M (Chiang et al. 2021). Meanwhile, Sun et al. (2020) suggested that the exponential dependence on metallicity in the Bolatto et al. (2013) prescription might overestimate α_{CO} in low-metallicity regions. Besides an exponential dependence, it is a commonly used strategy to formulate α_{CO} as a power-law of metallicity (e.g. Glover & Mac Low 2011; Schrubba et al. 2012; Hunt et al. 2015b). In this section, we examine how our findings might change with different α_{CO} prescriptions. Specifically, we will examine (1) how the correlation between ΔT_{clr} and D/G changes with α_{CO} (Sections 4.1 and 5.1), and (2) whether the D/G modification to the KS law still makes sense (Section 4.2).

We adopt three α_{CO} prescriptions here: a constant α_{CO} , an α_{CO} that depends on metallicity exponentially, and an α_{CO} that depends on metallicity with a power law. For the constant one, we adopt the α_{CO} in typical giant molecular clouds (GMCs) in the MW disc, $\alpha_{\text{CO}}^{\text{MW}} = 4.35 \text{ M}_{\odot} \text{ pc}^{-2} (\text{K km s}^{-1})^{-1}$ (Solomon et al. 1987; Strong & Mattox 1996; Abdo et al. 2010). We use the Bolatto et al. (2013) prescription (equation 14) for the exponential one. Lastly, we adopt the power-law prescription suggested by Accurso et al. (2017), who used the [C II] to CO $J = 1 \rightarrow 0$ ratio to constrain α_{CO} and obtained the following metallicity-dependent conversion factor:

$$\frac{\alpha_{\text{CO}}^{\text{A17}}}{1 \text{ M}_{\odot} \text{ pc}^{-2} (\text{K km s}^{-1})^{-1}} = 4.35 Z'^{-1.6}. \quad (\text{B1})$$

Note that we neglect the dependence on the offset from the main sequence in the Accurso et al. (2017) formulation, following the approach in Sun et al. (2020).

In addition to α_{CO} , we also examine how the variation in the CO line ratio, R_{21} (equation 1), might affect our results. We adopt the SFR-dependent formula proposed in Leroy et al. (2022, see their

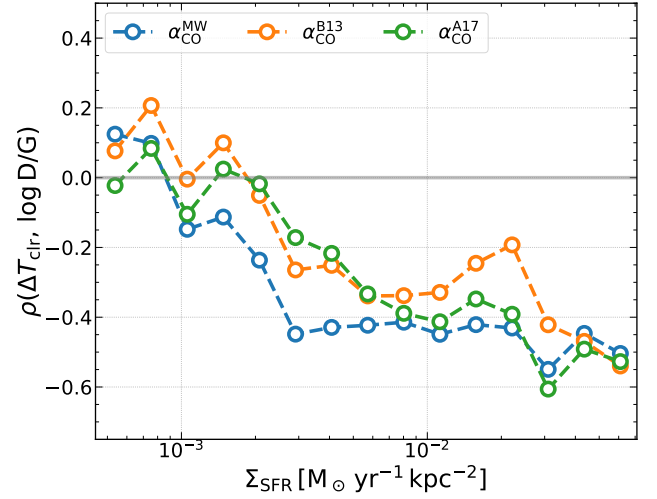


Figure B1. Pearson's correlation coefficient (ρ) between ΔT_{clr} and $\log(D/G)$ calculated with different α_{CO} prescriptions.

Table B1. The RMSD (in dex) of the power-law fittings to Σ_{SFR} using different sets of variables for the three α_{CO} prescriptions. For the fitting with two variables (Σ_{dust} and D/G), we examine two cases for R_{21} . See Section 4.2 for fitting formulation.

Formulation	$\alpha_{\text{CO}}^{\text{MW}}$	$\alpha_{\text{CO}}^{\text{B13}}$	$\alpha_{\text{CO}}^{\text{A17}}$
$\Sigma_{\text{SFR}} (\Sigma_{\text{dust}})$	0.27	--	--
$\Sigma_{\text{SFR}} (\Sigma_{\text{dust}}, \text{D/G}), \text{constant } R_{21}$	0.20	0.22	0.22
$\Sigma_{\text{SFR}} (\Sigma_{\text{dust}}, \text{D/G}), \text{varying } R_{21}$	0.22	0.24	0.24

Note: There is no α_{CO} involved in the $\Sigma_{\text{SFR}} (\Sigma_{\text{dust}})$ fitting.

Table 5), that is:

$$\log \left(\frac{R_{21}}{\langle R_{21} \rangle_{\text{gal}}} \right) = 0.129 \log \left(\frac{\Sigma_{\text{SFR}}}{\langle \Sigma_{\text{SFR}} \rangle_{\text{gal}}} \right) + 0.019, \quad (\text{B2})$$

where the $\langle \rangle_{\text{gal}}$ symbol represents the average value in the disc of each galaxy. For simplicity, we use $\langle R_{21} \rangle_{\text{gal}} = 0.65$ for all galaxies, and we adopt the geometric mean of the SFR surface densities for all pixels within a galaxy for $\langle \Sigma_{\text{SFR}} \rangle_{\text{gal}}$. Following the suggestion in Leroy et al. (2022), if the derived R_{21} is greater than 1.0, we directly set it to 1.0.

We first re-calculate the correlation between ΔT_{clr} (Section 4.1) and $\log(D/G)$ with the three α_{CO} prescriptions. The correlation coefficients are calculated for each Σ_{SFR} bin. Compared to Fig. 2, we only keep D/G because it is the only quantity affected by the choice of α_{CO} . As shown in Fig. B1, the correlation coefficients as a function of Σ_{SFR} have similar behaviours for the three α_{CO} prescriptions. They all show poor correlation at low Σ_{SFR} , and the correlations become stronger toward high Σ_{SFR} . The two metallicity-dependent α_{CO} prescriptions have similar transition Σ_{SFR} from poor to stronger correlation. Thus, as long as we use a metallicity-dependent α_{CO} , we expect T_{clr} to have poor correlation with D/G at low Σ_{SFR} . The correlations between ΔT_{clr} and $\log(D/G)$ calculated with varying R_{21} (equation B2) does not deviate significantly from the constant R_{21} results.

Next, we examine the power-law fittings to Σ_{SFR} similar to what we have done in Section 4.2 with $\alpha_{\text{CO}}^{\text{B13}}$. In Table B1, we present the RMSD of all the power-law fittings in this test. We test three formulations: the $\Sigma_{\text{SFR}} (\Sigma_{\text{dust}})$ and $\Sigma_{\text{SFR}} (\Sigma_{\text{dust}}, \text{D/G})$ with constant R_{21} , which we have performed in Section 4.2, and $\Sigma_{\text{SFR}} (\Sigma_{\text{dust}}, \text{D/G})$ with varying R_{21} in addition. As shown in Table B1, all the

three α_{CO} prescriptions show improved RMSD when moving from single-variable power law to the two-variable power law (constant R_{21}), indicating that the D/G-modification to the standard KS law (equation 21) is supported robustly against the change of the α_{CO} prescriptions. Meanwhile, the two-variable power law with varying R_{21} has systematically larger RMSD than the constant R_{21} ones, showing the variation of R_{21} does not improve the fitting.

When we interpret the two-variable power law as a D/G-modification to the standard KS law (equation 21) with different α_{CO} prescriptions, we find the coefficient for the $\log \Sigma_{\text{gas}}$ term (corresponding to the N value in the standard KS law) as 1.35 for $\alpha_{\text{CO}}^{\text{A17}}$ and 1.39 for $\alpha_{\text{CO}}^{\text{MW}}$, both lower than the 1.49 for $\alpha_{\text{CO}}^{\text{B13}}$. Meanwhile, we have similar coefficients for the $\log(\text{D/G})$ term for the metallicity-dependent prescriptions: 0.72 for $\alpha_{\text{CO}}^{\text{A17}}$ and 0.76 for $\alpha_{\text{CO}}^{\text{B13}}$. On the other hand, the coefficient for the constant $\alpha_{\text{CO}}^{\text{MW}}$ is 0.48, which yields a weaker correction than the metallicity-dependent α_{CO} prescriptions.

This paper has been typeset from a \LaTeX file prepared by the author.